

Review

State of the Art and Trends in Wind Resource Assessment

Oliver Probst * and Diego Cárdenas

Physics Department, Instituto Tecnológico y de Estudios Superiores de Monterrey, Monterrey, N.L., CP64849, Mexico; E-Mail: diego.cardenas@itesm.mx

* Author to whom correspondence should be addressed; E-Mail: oprobst@itesm.mx;
Tel.: +52-81-8358-2000 Ext. 4631; Fax: +52-81-8358-2000 Ext. 4632.

Received: 1 April 2010; in revised form: 4 May 2010 / Accepted: 21 May 2010 /

Published: 3 June 2010

Abstract: Given the significant rise of the utilization of wind energy the accurate assessment of the wind potential is becoming increasingly important. Direct applications of wind assessment techniques include the creation of wind maps on a local scale (typically 5-20 km) and the micrositing of wind turbines, the estimation of vertical wind speed variations, prospecting on a regional scale (>100 km), estimation of the long-term wind resource at a given site, and forecasting. The measurement of wind speed and direction still widely relies on cup anemometers, though sonic anemometers are becoming increasingly popular. Moreover, remote sensing by Doppler techniques using the backscattering of either sonic beams (SODAR) or light (LIDAR) allowing for vertical profiling well beyond hub height are quickly moving into the mainstream. Local wind maps are based on the predicted modification of the regional wind flow pattern by the local atmospheric boundary layer which in turn depends on both topographic and roughness features and the measured wind rose obtained from one or several measurement towers within the boundaries of the planned development site. Initial models were based on linearized versions of the Navier-Stokes equations, whereas more recently full CFD models have been applied to wind farm micrositing. Linear models tend to perform well for terrain slopes lower than about 25% and have the advantage of short execution times. Long-term performance is frequently estimated from correlations with nearby reference stations with concurrent information and continuous time series over a period of at least 10 years. Simple methods consider only point-to-point linear correlations; more advanced methods like multiple regression techniques and methods based on the theory of distributions will be discussed. Both for early prospecting in regions where only scarce or unreliable reference

information is available, wind flow modeling on a larger scale (mesoscale) is becoming increasingly popular.

Keywords: Anemometry; vertical profiling; measure-correlate-predict; wind mapping; CFD; mesoscale

1. Introduction

The utilization of wind energy has evolved in recent decades from a marginal activity motivated mainly by local concerns for a cleaner environment and initiatives by municipalities and interested individuals into a multi-billion dollar industry. In 2008, the wind energy industry directly employed 108,000 people in Europe alone [1]; if indirect jobs are considered as well, this number increases to 154,000 [1]. In the US, it has been estimated that about 85,000 jobs were directly or indirectly related to the wind energy industry [2]. The estimated annual turnover of the global wind energy industry is over € 12 billion [3]. Investments in wind farms, at a typical overall cost of US\$2,000 per installed kW [4], require quite substantial funds even for small projects, while wind parks of several hundreds of MW are becoming common in many parts of the world, particularly the US [2]. It is clear from the above that an accurate estimate of the expected energy production figures together with an approximation of the different uncertainties associated with the project is required to secure funds and hedge risks. The assessment of the wind resource enters the project development arena in several stages: (1) Early prospecting of suitable sites, (2) wind mapping at the potential site and conceptual wind farm design, (3) micro-siting of turbines and optimization, (4) risk assessment, (5) planning of certification towers, (6) post-construction performance analysis, (7) operation. As in other fields of engineering, the higher the knowledge of the system, the smaller the safety margins and, therefore, the higher the potential returns on the investment. An accurate prediction and validation of the performance of a potential wind farm is therefore vital for the success of a project.

2. Anemometry and Remote Sensing

Nowadays a series of measurement techniques is available for on-site wind resource measurement ranging from point measurements performed at different heights using cup anemometers (Figure 1) [5] or ultrasonic sensors [6] to profiling techniques like SODAR (Figure 1) [7-9] or LIDAR [10-12]. Until now, the overwhelming majority of measurement campaigns for commercial wind farms rely on cup anemometry and occasionally on ultrasonic sensors, where the latter is often preferred in research applications. Remote-sensing techniques like SODAR or LIDAR are increasingly explored as a complementary approach, particularly in large wind farm projects where the profiling device can be conveniently relocated within the project area for an exploration of the wind resource at different sites, following an initial calibration period where the profiler is operated in conjunction with a conventional tower-based measurement system.

Figure 1. Photographs of (a) a tower-based measurement system with three redundant sets of cup anemometers at three heights, (b) a SODAR unit on a trailer and equipped with a photovoltaic power system.



2.1. Cup anemometry

A cup anemometer [5-8] is a simple device relying on the different aerodynamic drag of the convex and concave surfaces of a suitably designed cup. Typically two to four cups are mounted symmetrically on a vertical axis and allowed to rotate freely. If placed in a constant speed air stream, the anemometer will eventually spin at a frequency proportional to the wind speed. If coupled to a small electric synchronous generator, the corresponding electrical signal can be conveniently registered by data conditioning and logging. Generally, since only the frequency information of the signal is of interest, a signal forming device is required for processing in digital data loggers, as the amplitude of the signal inconveniently varies proportionally to the frequency. A common choice is to convert the analog signal into a train of fixed amplitude pulses which can be counted by the digital device.

The theory of operation can be illustrated easily in the case of a two-cup anemometer. Neglecting friction, the change in angular momentum L is given by the accelerating torque M caused by the different drag coefficients $C_{d,v}$ and $C_{d,x}$, respectively [5,8]:

$$\frac{dL}{dt} = I \frac{d\Omega}{dt} = M = \frac{1}{2} \rho A R \left\{ C_{d,v}(\phi)(U - \Omega R)^2 - C_{d,x}(\phi)(U + \Omega R)^2 \right\} \quad (1)$$

where I is the moment of inertia of the device, Ω is the rotational frequency, A the projected area and $\Omega = d\phi/dt$. Although the drag coefficient varies with the azimuthal angle ϕ during one half-period of rotation, it is generally assumed that they can be replaced by average values, simplifying the analysis considerably. If the velocity ratio λ and the drag ratio μ are defined by

$$\lambda = \frac{\Omega R}{U} \quad \text{and} \quad \mu = \frac{C_{d,v}}{C_{d,x}} \quad (2)$$

we have for the steady-state case:

$$\lambda = \frac{\mu + 1}{\mu - 1} - \sqrt{\left(\frac{\mu + 1}{\mu - 1} \right)^2 - 1} \quad (3)$$

i.e., the rotational frequency is proportional to the wind speed, where the proportionality constant is a function of the drag ratio. For typical values of the drag coefficients for the concave and convex surfaces of 1.4 and 0.4, respectively, the steady-state speed ratio is calculated to be 0.303, *i.e.*, the cups will rotate at about a third of the wind speed.

The equations above assumed the wind speed to be uniform horizontally. If a horizontal wind shear is considered, then corrections have to be applied to the apparent wind speeds at the concave and convex surface, respectively. As an example, we observed that a 0.2% asymmetry in the horizontal wind speed produces a 0.7% change in the steady-state speed ratio [8]. Even though in free stream little asymmetry can be expected on the length scale given by the typical anemometer size ($R \sim 0.1\text{m}$), the proximity of the anemometer to the measurement tower and the influence of the mounting booms may well incur a sizeable change in the calibration factor of the anemometer, particularly if the booms are short and the cups are not properly separated from their mounting base.

In the above paragraphs we assumed a constant in-flow wind speed which is hardly ever encountered in field measurements. If dynamic variables of the wind field are of interest, such as the turbulent kinetic energy or gusts in wind speed, then the inertia of the anemometer has to be taken into account. The finite response time of the sensor will also have an impact on the average wind speed, particularly in turbulent environments. In order to explore the effect of changes in wind speed, we first observed that a generalization of Equation (1) can be put in the form [5]

$$\frac{d\Omega}{dt} = -aU\Omega + bU^2 + c\Omega^2 \quad (4)$$

Generally, the last term can be neglected, allowing to obtain an analytical solution and evaluate the step response of the anemometer. If an initial wind speed of U_0 is assumed, changing abruptly to $U_1 = U_0 + \Delta U$ at a time $t = 0$, then the change in wind speed as a function of time is given by [5]

$$\Omega(t) = \frac{b}{a} [U_0 + \Delta U \{1 - \exp(-t/\tau)\}] \quad (5)$$

where the time constant is given by

$$\tau = \frac{1}{aU_1} = \frac{L_a}{U_1} \quad (6)$$

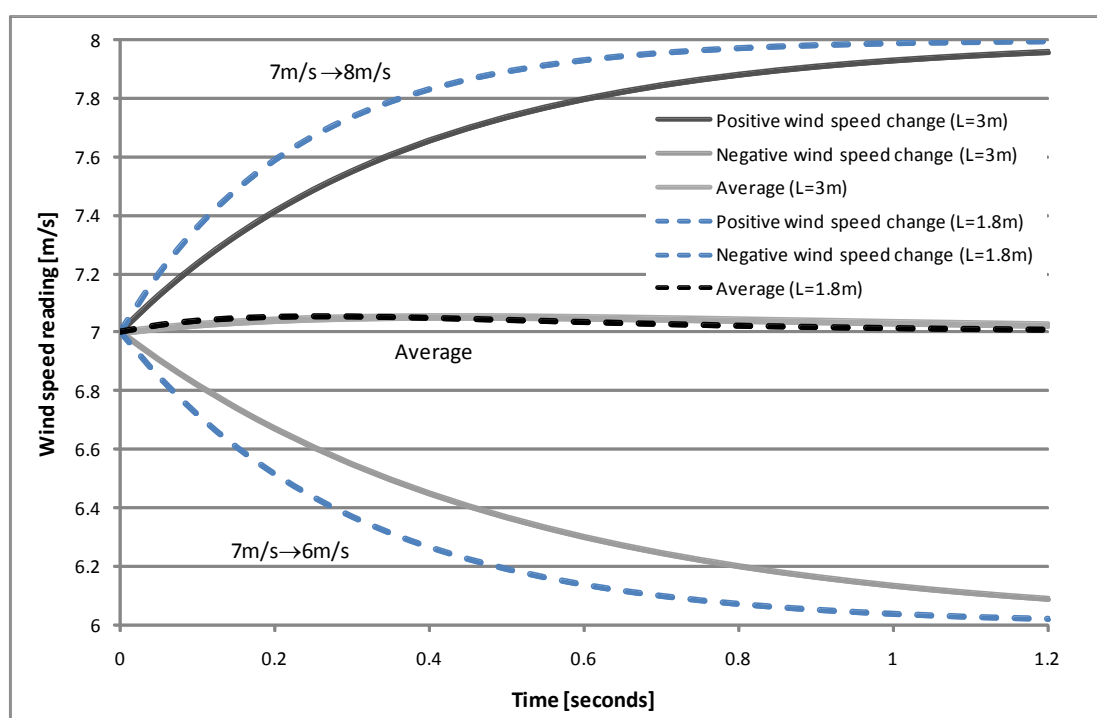
In Equation (6) we have introduced the *distance constant* L_a of the anemometer, which is only a property of the instrument itself and does not depend on the wind speed signal, as opposed to the time constant which is inversely proportional to the value of the final wind speed. In principle, the distance constant could be measured in a wind tunnel subjecting the anemometer to a step change, say from zero to a finite value of the wind speed. However, in practice, most of the increase in rotational frequency typically occurs during the first three full rotations, so the determination of L_a from a fit of the experimental data to Equation (5) becomes very imprecise. Kristensen and Hansen [5] proposed an alternative to compare the field response of the cup anemometer under observation with an ultrasonic anemometer, the time response of which is significantly faster than the one of the cup anemometer. The cup anemometer transfer function, determined theoretically as

$$T(\omega) = \frac{1}{1 + L_a^2(\omega/U)} \tag{7}$$

can then be calculated from the ratio of the spectra measured by the cup and the sonic anemometer, respectively. For the research anemometer RISO P2546 a distant constant of $L_a = 1.8$ m was found [5]. A commercial anemometer may have larger values of up to about 3 m.

The fact that the time response of a cup anemometer is determined by a distance length rather than a time constant has a direct implication on the accuracy of the measurements under the typical fluctuating wind speed conditions. This point is illustrated in Figure 2 where the step response of two anemometers, one with a distance constant of 1.8 m (typical of the RISO P2546) and another with a length of 3m (representative of commercial anemometers like the NRG #40 max often used for wind farm development), is shown for positive and negative wind speed changes. Although the two sets of curves look symmetric at first sight, averaging the curves reveals that the anemometer actually reacts faster to a positive rather than a negative wind speed change; this phenomenon is termed *overspeeding*. In the case of Figure 2, it can be seen that the maximum deviation of the average curve from the horizontal line is about 0.05 m/s for both curves. However, the average deviation is less than 0.03m/s for the anemometer with a distance constant of 1.8 m, where the 3m-anemometer has an average overspeeding during the 1.2s-interval shown in Figure 2 of almost 0.04 m/s.

Figure 2. Illustration of the different response of a cup anemometer for positive and negative wind speed changes, respectively, for two values of the distant constant (1.8 m and 3 m).



An important point to consider is anemometer calibration [8]. While uncalibrated anemometers have been used for quite some time, e.g., the popular NRG #40 max anemometer, individual calibration is now the standard in the wind energy industry. The uncertainty of uncalibrated

anemometers is due both to the error sources in the generic calibration procedure and the scatter between units caused by fluctuations in the production process. A typical uncertainty value of an uncalibrated anemometer is of the order of 1.4%, while individually calibrated anemometers may be expected to have an uncertainty of the order of 0.7%.

It should be noted, however, that calibration uncertainty is generally not the most important error source for the long-term estimation of the wind resource and turbine yield, respectively, at a given site. An appropriate mounting scheme [8] providing near-free stream conditions for the anemometer under prevailing wind conditions is as important as the anemometer calibration. If possible, the highest anemometer on a measurement tower should be mounted on top of the tower and unobstructed by structural elements or lightning spikes. If this measurement does not occur at hub height (typically 80 m) but at a lower height, then the assessment of the hub height wind speed will rely on a vertical extrapolation requiring wind speed sensors at different heights (see Section 3). This extrapolation procedure may cause an uncertainty of the same order as the calibration uncertainty, if the sensors at different heights are not mounted under identical exposure conditions. Tower wake effects (Section 2.4) can be assessed by comparing records from two anemometers at the same level (generally the greatest height) and often cause a smaller uncertainty than anemometer calibration, due to the systematic nature of the wake effect. While other sources of uncertainty have to be considered in the course of a wind project feasibility study, the largest uncertainty generally comes from inter-annual variations of the local climatology (see Section 4 on long-term assessment).

As opposed to ultrasonic sensors described in the following section, anemometers do not provide information about either wind direction or temperature, so they have to be complemented by corresponding sensors. Wind direction is generally measured by a vane, the direction of which is determined by a voltage divider. Temperature is often measured by integrated circuit sensors; a radiation shield is always indispensable to avoid heating by solar radiation. While the effect of atmospheric pressure on air density can generally be approximated by the value of the barometric formula for the given site altitude, the effect of temperature is more substantial; temperature measurements are therefore always part of a wind measurement campaign. Finally, relative humidity variations can often be neglected.

2.2. Ultrasonic sensors

Sonic anemometers [7,9-11] measure the wind speed in two or three dimensions based on a comparison of the times-of-flight of two anti-parallel sonic pulses. In modern sonic anemometers each measurement path consists of a pair of transducers, each of them capable of both transmitting and receiving. For a uniform and stationary wind field the wind velocity component in the direction of the measurement path can then be calculated from [7,9,11]

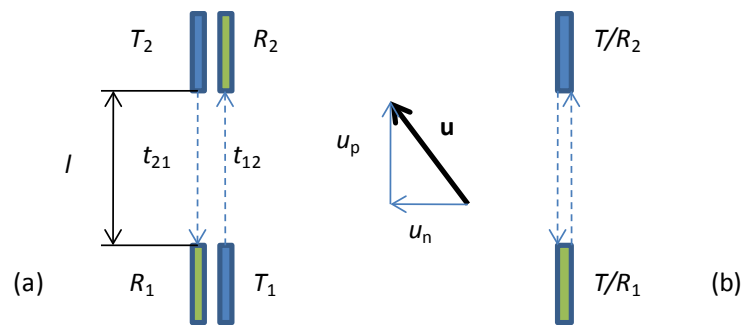
$$u_M = \frac{l}{2} \left(\frac{1}{t_{12}} - \frac{1}{t_{21}} \right) \quad (8)$$

where t_{12} and t_{21} are the flight times from transceiver 1 to 2 and vice versa, and l is the distance between the transceivers; see Figure 3. Two or three orthogonal measurement paths can be combined in one instrument, in order to measure the full wind velocity vector. In principle, sonic anemometers

have a series of advantages over cup anemometers, such as the absence of moving parts, allowing a faster response to fluctuations and avoiding overspeeding. Furthermore, their response is linear over a large range of frequencies, and the measurement is relatively independent of the flow properties, such as spatial and time variations, temperature, density *etc.* Finally, sonic anemometers are absolute instruments that do not require individual calibrations [7]. Some drawbacks do exist, such as the influence of the finite measurement path, path separation, and transducer shadows.

Figure 3. Geometry of ultrasonic transceiver arrangements (one measurement path).

(a) Separate transmitters / receivers for each direction, (b) integrated transceiving units.



In order to determine how the measured wind velocity component relates to the actual line-averaged wind speed along the measurement path we observe that the flight times t_{12} and t_{21} can be calculated from [9,11]

$$t_{12} = \int_{p_1}^{p_2} \frac{dp}{c + u_p(p,t)} \tag{9}$$

$$t_{21} = \int_{p_1}^{p_2} \frac{dp}{c - u_p(p,t)} \tag{10}$$

where $u_p(p,t)$ is the instantaneous wind speed at a position p between the path extremes p_1 and p_2 at a time t (see Figure 3) Both pulses are assumed to have been fired simultaneously. If the wind is constant in space and time ($u_p(p,t) = u$), then equation (8) correctly predicts $u_M = u$. In the case of a wind field varying in space and time, however, it can be expected that the fluctuations will contribute to the measured wind speed value. Using perturbation theory, Cuerva and Sanz-Andrés [11] derive an expression for the measured wind speed in the general case of a fluctuating wind field:

$$u_M = u \left(1 + \frac{1}{2} \varepsilon (F^+ + F^-) \right) \tag{11}$$

where ε measures the strength of the perturbation and F^+ and F^- account for the differences in traveling time:

$$F^\pm = \int_0^1 \delta(P, T_0^\pm(P)) dP \tag{12}$$

P is the position within the measurement path normalized to the path length, δ the relative variation of the wind speed and T_0^\pm the travel times in either direction in the absence of the perturbation. As an example of the theory, Cuerva and Sanz-Andrés discuss the effect of an oscillating measurement mast

in response to, e.g., vortex shedding. For an oscillating tower with an angular frequency ω the relative measurement error is found to be

$$\frac{u_M - u}{u} = \frac{\varepsilon \omega l}{2c} \cos(\omega t_0) \tag{13}$$

where t_0 is the time delay between the maximum of the oscillation and the pulse emission. Note that for typical values of the shedding frequency of a few Hz $\omega l/c \ll 1$, so that $\varepsilon \omega l/c$ is a second order small quantity. Moreover, for a random phase distribution for the vortex shedding process, the average of the cosine function will be zero for typical data logger averaging intervals in the range of 1 to 10 minutes.

In order to discuss the operation of sonic anemometers under realistic atmospheric conditions Cuerva and Sanz-Andrés first describe the fluctuating component of the wind speed by a Fourier-Stieltjes integral [11]

$$u_i(\mathbf{x}, t) = \int_{-\infty}^{\infty} e^{i\mathbf{k}\cdot\mathbf{x}} d\Psi_i(\mathbf{k}, t) \tag{14}$$

with a wave vector \mathbf{k} with components $k_1, k_2,$ and k_3 in the three orthogonal directions of the wind velocity coordinate system. $\Psi_{ij}(\mathbf{k}, t)$ are random functions which can be related to the spectral density tensor $\Phi_{ij}(\mathbf{k})$ by

$$\overline{d\Psi_i(\mathbf{k}, t) d\Psi_j(\mathbf{k}', t)} = \begin{cases} 0 & \mathbf{k} \neq \mathbf{k}' \\ \Phi_{ij}(\mathbf{k}) d\mathbf{k} & \mathbf{k} = \mathbf{k}' \end{cases} \tag{15}$$

where

$$\Phi_{ij}(\mathbf{k}) = \frac{E(\mathbf{k})}{4\pi k} (k^2 \delta_{ij} - k_i k_j) \tag{16}$$

and $E(\mathbf{k})$ is the three-dimensional spectrum which can be expressed as [12]

$$E(\mathbf{k}) = \varepsilon^{2/3} k^{-5/3} \tag{17}$$

provided an inertial sub-range exists in the wave-number range of interest. In order to relate the spectrum of the random fluctuations to measurable quantities, the so-called one-dimensional spectra for a given component, say k_1 , can be obtained by integrating over the remaining coordinates:

$$F_{ij}(k_1) = \int_{-\infty}^{\infty} \int_{-\infty}^{\infty} \Phi_{ij}(k_1, k_2, k_3) dk_2 dk_3 \tag{18}$$

This tensor is the Fourier transform of the velocity correlation tensor for separation in the longitudinal direction. It can now be calculated both for ideal conditions and considering the measurement conditions using the framework of Equations (16) and (17), in order to define a transfer function R_{ij} by setting

$$R_{ij}(k_1) = F_{ij}^M(k_1) / F_{ij}(k_1) \tag{19}$$

where F_{ij}^M is the one-dimensional spectrum determined for the wind velocity as measured by the sonic anemometer. If the special case of an alignment of the measurement path with one of the components of the wind velocity, say x , is considered, then the corresponding transfer function R_{11} can be calculated as follows [11]

$$R_{11}(k_1) = \frac{1}{4} \left\{ \sin c(+)^2 + \sin c(-)^2 + 2 \cos \left[k_1 l \left(\frac{M_\infty^2}{(1-M_\infty)^2} + Z_B \right) \right] \sin c(+)\sin c(-) \right\} \quad (20)$$

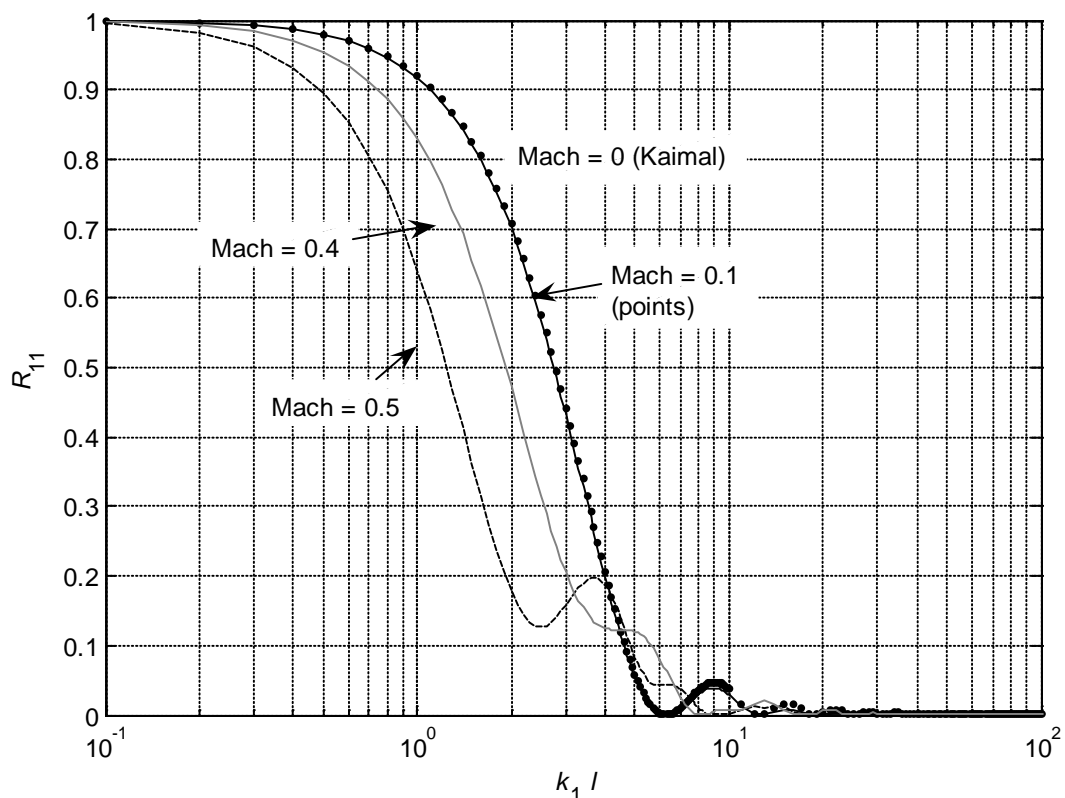
where

$$\sin c(\pm) = \frac{\sin[(k_1 l / 2) / (1 \pm M_\infty)]}{(k_1 l / 2) / (1 \pm M_\infty)} \quad (21)$$

M_∞ is the Mach number of the free-stream wind speed, l the length of the measurement path as before, and Z_B is the non-dimensional delay time between pulse shots. For practical purposes, R_{11} can be interpreted as a transfer function of the sonic anemometer [11,12], measuring the response of the instrument to a turbulent perturbation with wave number k_1 .

As seen in Figure 4, where the longitudinal transfer function R_{11} has been plotted for different Mach numbers under the assumption of simultaneous emission of both measurement pulses, the influence of the Mach number on the instrument response is negligible for wind speeds in the interesting range, since even for a Mach number of 0.1 (equivalent to a wind speed of 34.5 m/s) the response function is essentially identical to the one for $M_\infty = 0$ (labeled as “Kaimal” in Figure 4). Not unexpectedly, for very large wind speed values the finite speed of sound becomes a limiting factor, reducing the spatial frequencies that can be resolved with the instrument. The fact that often the two opposite sound pulses are fired in a sequential manner, which gives rise to a finite delay time, does have an important impact on the instrument response. This can be seen in Figure 5, where the response function has been plotted for different values of the normalized delay time.

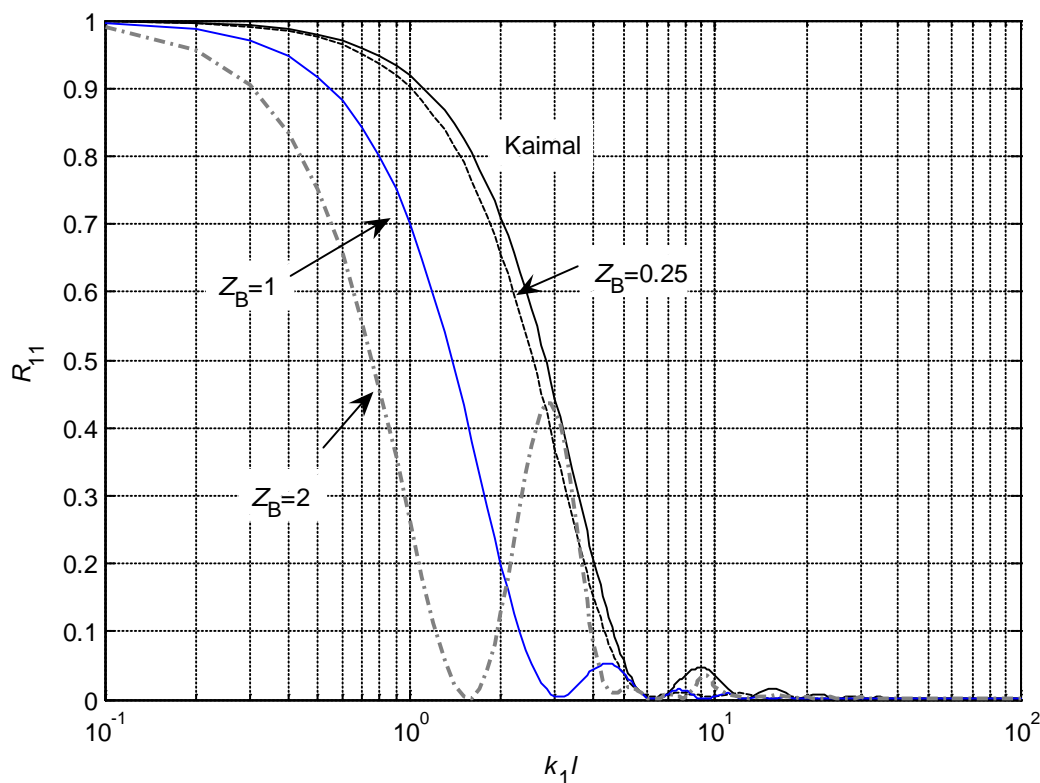
Figure 4. Transfer function of a sonic anemometer for different Mach numbers as a function of the dimensionless spatial frequency $k_1 l$. The non-dimensional delay time is $Z_B = 0$ for all curves.



2.3. Sonic detection and ranging (SODAR)

While anemometers (both mechanical and sonic) measure wind velocity at a specific location in space, requiring the use of several instruments for the assessment of vertical profiles, remote sensing techniques are capable of providing an almost instantaneous photograph of the complete vertical wind velocity profile up to a certain height. One such technique, becoming increasingly popular in the wind energy industry, is SODAR (Sonic Detection And Ranging) [13-17]. SODAR was originally developed for atmospheric research [13-15] and air traffic safety but is increasingly deployed where a knowledge of the wind velocity profile up to greater heights than provided by anemometer towers (generally limited to 60 m or 80 m) is required, or the assessment of different locations within a vast wind project development is desirable. Commercially available systems tailored for wind resource assessment are capable of providing information on the atmospheric boundary layer up to heights of 200 m or 300 m, thereby covering the full range of heights swept by typical rotor blades. This type of information is particularly useful when dynamic structural analysis of the turbine rotor is performed, since both wind shear over the rotor diameter and the evolution of turbulence with height significantly impact on the prediction of rotor stress, and their precise knowledge avoids the use of sometimes oversimplifying assumptions.

Figure 5. Transfer function of a sonic anemometer as a function of the dimensionless spatial frequency $k_1 l$ for different normalized delay times. $M_\infty = 0.1$ except for the Kaimal case ($M_\infty = 0$) shown for reference purposes.



The measurement principle of SODAR relies on the backscattering of an audible sonic beam at a given frequency (typically in the range from 2000 to 4500 Hz) from inhomogeneities within the atmosphere and the detection of a slight frequency change caused by the moving scatter volume on account of the Doppler effect [16]. Since first-order modifications of the carrier frequency only occur

in the direction of the beam, three independent beams are required to determine the velocity components in the vertical and two horizontal directions. While the vertical component can be determined by sending a beam straight up into the atmosphere, the determination of the horizontal components (generally priority for wind resource assessment) requires the corresponding beams to be tilted. If (u, v, w) are used to denominate the $x, y,$ and z components of the wind velocity, respectively, S denotes the speed of sound, f_0 the frequency at which the sonic beam is emitted and Δf the frequency shift registered upon receiving the backscattered signal, then the following relationships hold [16]:

$$w = \frac{-\Delta f S}{2f_0} \quad (22)$$

$$v = \frac{-\Delta f S}{2f_0 \sin \theta_y} - \frac{w}{\tan \theta_y} \quad (23)$$

$$u = \frac{-\Delta f S}{2f_0 \sin \theta_x} - \frac{w}{\tan \theta_x} \quad (24)$$

θ_x and θ_y are the tilt angles for the x - and y -beams respectively. The power levels of the backscattered signals are very low, as can be seen from the following equation, termed the SODAR equation [18]:

$$P_R = P_T G A_e \sigma_s \frac{c \tau e^{-2\alpha z}}{2 z^2} \quad (25)$$

where P_R and P_T are the receive and transmit power, respectively, G is the antenna transmit efficiency, A_e the effective receive area, σ_s the cross section for turbulent scattering of sound in air per unit volume and unit solid angle, c the speed of sound, τ the pulse length, α the sound absorption coefficient and z the measurement height. The scattering cross section can be calculated from [19]

$$\sigma_s = 0.016 k^{1/3} C_T^2 / (4T) \quad (26)$$

where C_T^2 is the structure function coefficient for temperature fluctuations defined as [20]

$$C_T^2(\mathbf{r}) = \frac{(\Theta(\mathbf{r}_0) - \Theta(\mathbf{r} + \mathbf{r}_0))^2}{r^{2/3}} \quad (27)$$

Θ is the potential temperature, *i.e.*, the temperature a volume of air at temperature T would have if expanded adiabatically to standard pressure (100 kPa). \mathbf{r} and $\mathbf{r} + \mathbf{r}_0$ are the position vectors of two locations in the atmospheric boundary layer and the temperature structure function is assumed to depend only on the difference vector \mathbf{r} of the two positions.

As illustrated in Figure 6, commercial sodar units designed for wind energy applications are capable of obtaining reliable wind speed and direction readings for heights of up to 250 m, well beyond the maximum height swept by the rotor blades; the measurements shown were obtained with an Atmospheric Research and Technology (ART) Model VT-1 unit. It is conspicuous, from the example, how significant deviations from the logarithmic profile can occur well below the height of the atmospheric boundary layer; such measurements therefore provide useful input for the calculation of the effective rotor-averaged wind speed and the mechanical stresses occurring in the rotor blades. In Figure 7 a comparison is shown between the readings of a cup anemometer at 54 m height and the

sodar vector wind speed obtained for 50 m at an unobstructed flat site, demonstrating the excellent correlation between the two.

Figure 6. Vertical wind speed and direction profiles as measured with a single frequency three-beam sodar device. *Data courtesy of Atmospheric Research and Technology, Inc. [21].*

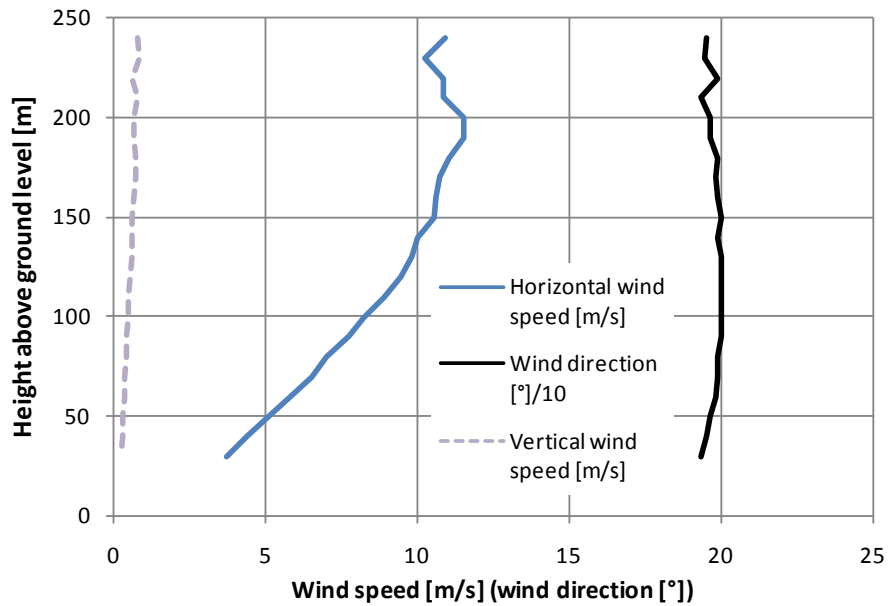
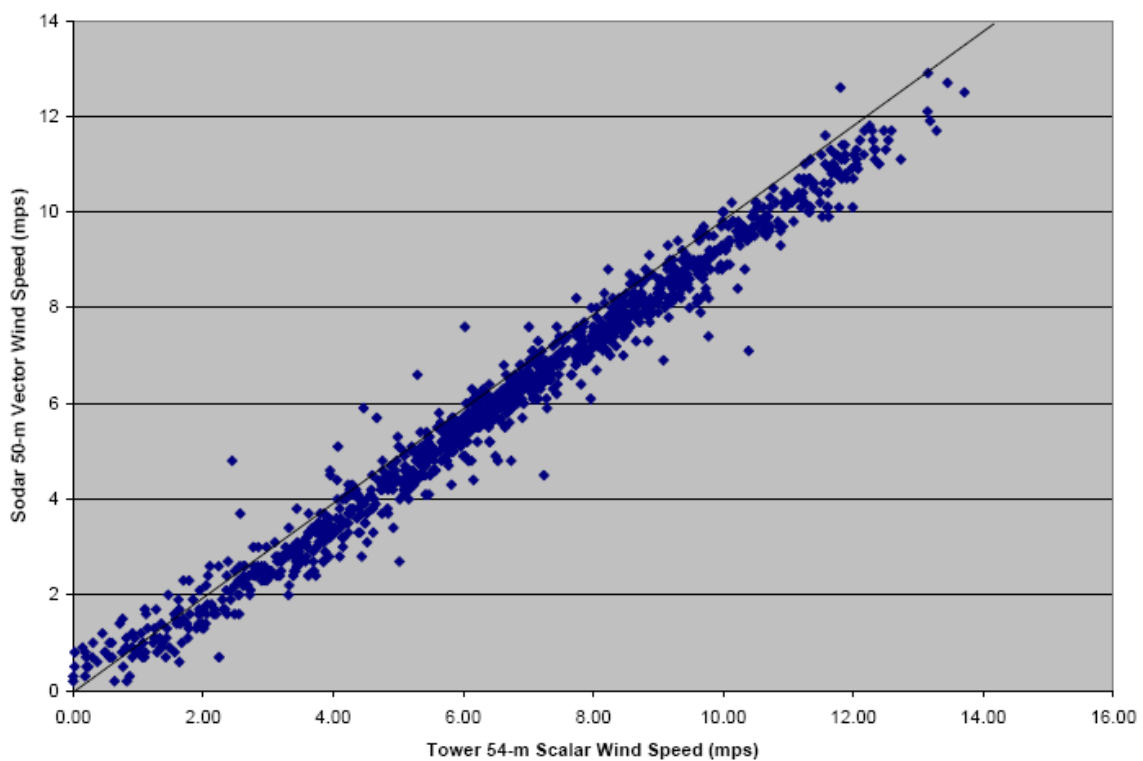


Figure 7. Scatter plot showing the correlation of the sodar-measured (vector) wind speed at 50 m and the anemometer-measured (scalar) wind speed at 54 m above ground level. *Courtesy of Atmospheric Research and Technology, Inc. Reproduced with permission [21].*



In several studies the application of SODAR for wind speed measurements has been discussed [23-26]. The general approach is to correlate the SODAR data to concurrent tower data recorded at a site close enough to the SODAR location to make sure the same wind field is probed. On the other hand, one has to allow for a certain distance between tower and SODAR to avoid static echo interference stemming from reflections of the SODAR beam at the tower structure, even when the SODAR beams are pointing away from the tower. While the manufacturers recommend that any significant obstacle should be seen by the SODAR at an angle of 45° or less, in our experience the minimum distance should be closer to two obstacle heights in order to avoid anomalous wind shear readings indicative of echo effects. In general, the key to a successful utilization of SODAR for wind resource assessment lies with the appropriate filtering of the raw data, since the SODAR signal is easily affected by background noise and echo signals due to reflections from static obstacles, simulating a zero wind speed event occurring at a height equivalent to the round-trip travel time of the SODAR beam. Background noise issues can often be dealt with satisfactorily by establishing data rejection criteria based on minimum values of signal amplitude and/or signal-to-noise ratio. While reflections from hard surfaces are detected relatively easily with the echo rejection algorithms implemented in commercial SODAR devices, reflections from softer surfaces such as vegetation, hills and low buildings are more subtle to detect. Since clutter affects lower range gate data more strongly, they also have an adverse effect on the determination of wind shear, if not properly accounted for [25]. A pragmatic approach, recommended by SODAR manufacturer ART, is to use a short (6 m) pole with a conventional anemometer, the readings of which can be correlated to the SODAR readings for quality control when no external mast is available [24].

2.4. Light detection and ranging (LIDAR)

Much like SODAR, modern LIDAR (Light Detection And Ranging) devices designed for wind energy purposes rely on the detection and frequency analysis of backscattered waves [27,28,29]. As in SODAR, the wind velocity component along with the observation direction is obtained through a Fast Fourier Transformation (FFT) of a Doppler-shifted signal. However, instead of sound waves laser beams are used and backscattering is caused by interaction with particles (aerosols) and molecules in the atmosphere instead of density fluctuations as in the case of SODAR. Scattering mechanisms include molecular processes such as Rayleigh (elastic) and Raman (inelastic) scattering, with Rayleigh scattering being by far the dominant process. Interaction with particles is also known as Mie scattering. For eye safety, commercial units use infrared laser light at a wavelength of $1.55 \mu\text{m}$ [27].

In order to obtain the three vector components of the wind velocity, the laser beam has to be inclined at an angle θ with respect to the normal, much like in SODAR units. As opposed to SODAR, however, where beam steering relies on phase shifts between the speaker units contained in the antenna, requiring a relatively complex electronic control scheme, laser beams can be easily rotated by means of a rotating wedge, in order to acquire redundant information by performing a full 360° scan around the vertical axis.

The line-of-sight velocity component obtained from the Doppler shift of the laser frequency then becomes a function of the azimuth angle ϕ with the general form [27]

$$v_{\text{LOS}}(\phi) = \frac{\lambda_0 \Delta f_{\text{Doppler}}(\phi)}{2} = |a \cos(\phi - b) + c| \tag{28}$$

where the parameters a , b , and c can be obtained from a non-linear least-square fit to the experimental data. From the geometry of the arrangement we can then calculate the wind velocity components according to

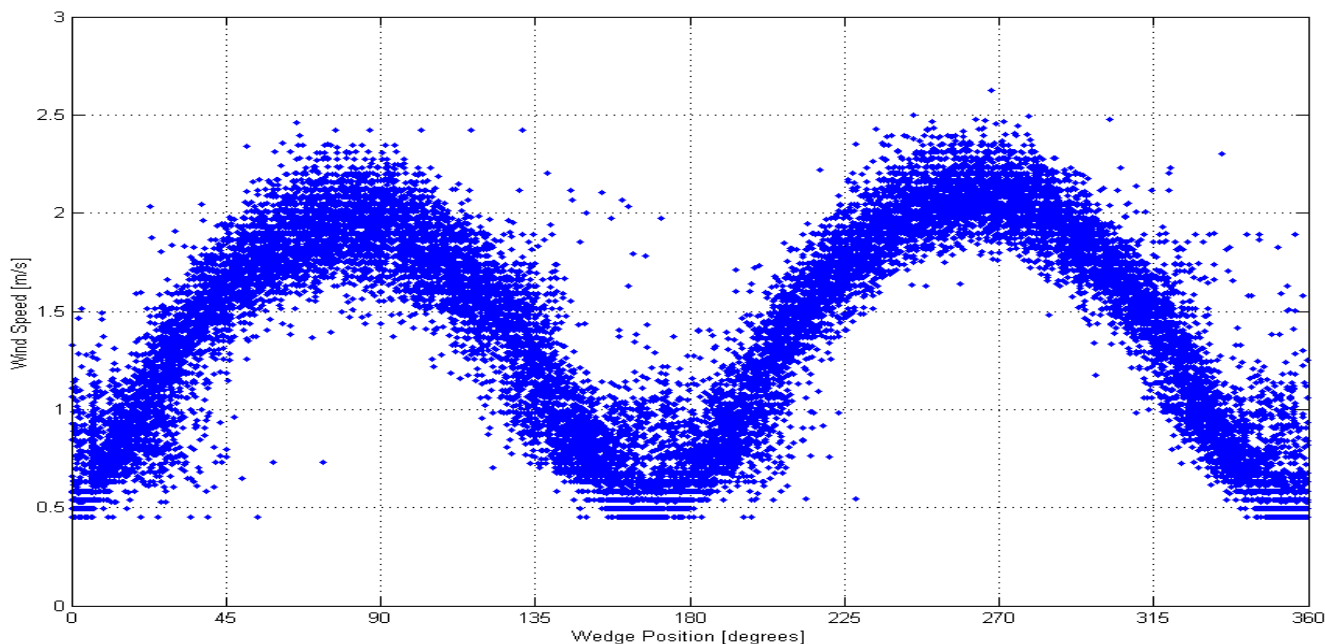
$$u = \frac{a}{\sin \theta} \tag{29}$$

$$w = \frac{c}{\cos \theta} \tag{30}$$

$$\text{wind direction} = b \pm 180^\circ \tag{31}$$

where a 180° wind bearing ambiguity can occur in the case of a poor fit of Equation (28) to the data. In this case, an additional wind direction sensor used in conjunction with the LIDAR unit can be used to resolve this ambiguity. An example of the azimuthal variation of the line-of-sight velocity is shown in Figure 8 [30].

Figure 8. Line-of-sight velocity determined with a LIDAR unit as a function of the azimuth angle [30]. *Reproduced with permission [31].*



Much like sodar, LIDAR requires a finite angle θ in order to obtain a reliable reading for the horizontal wind velocity component; in the case of the commercial unit ZephIR [27] an angle of $\theta = 30^\circ$ is used. A natural consequence of this arrangement are significant volume averaging effects, with increasing volumes at higher sampling heights. As opposed to SODAR where the beam sample different and often disjunct volumes, the averaging process at a LIDAR unit covers a 360° azimuthal range, so all three wind velocity components belong to the same averaging volume.

In spite of the large averaging volumes, published comparisons of LIDAR measurements with tower-based anemometer measurements generally find a high degree of correlation ($R^2 = 0.95$ and higher), with better correlations for wind speed averages than for their standard deviations. Jaynes *et al.* [27] find the correlations are limited more by uncertainty sources at the reference tower than at the LIDAR, where most of the error sources could be traced back to interference with the tower structure. Due to encouraging initial experiences and despite its relatively high cost it can be expected that LIDAR units will play an increasingly important role for wind resource assessment and wind turbine performance certification.

The major obstacle for a more widespread utilization of LIDAR units for routine wind resource assessment is currently the high cost of the units (typically priced at around US\$150,000), compared to US\$50,000 for common SODAR units and some US\$25,000 for an instrumented 60 m tower. Due to the high price of LIDAR units, leasing units for special purpose campaigns is a suitable commercial alternative pursued by some providers. One possible application could be comparative studies, where the unit is placed at a prospective location for a limited period of time (1–3 months) and the long-term wind resource is determined through correlations with a near-by anemometry tower. Another useful applications include turbine certification campaigns under the IEC 61400-12 standard. In the long run LIDAR units can be expected to play a major role in routine wind resource assessment.

2.5. Tower shading effects

When wind speed measurement instruments are mounted on a tower, they are inevitably affected to some degree by flow distortion [8,32]. The minimization of such effects therefore requires a certain knowledge of the general flow characteristics around the tower, apart from common-sense guidelines as to the mounting of the measurement devices. Two general types of towers are commonly used: (1) Tubular towers with tower diameters in the 20–25 cm range (for typical heights of 60 m), (2) lattice towers with either triangular or square sections and similar diameters as in the case of tubular towers. Tubular towers are suitable for erection by up-tilting by means of a ginpole and therefore do not require staff with tower climbing skills. Lattice towers are often an appropriate solution in places where an antenna construction and installation industry (generally for telecommunications applications such as radio and cellular telephony) exists.

The effect of the tower on the distortion of the flow field can be modeled by computational fluid dynamics (CFD) techniques, where, in the case of lattice towers, it is necessary to combine Navier-Stokes modeling with actuator disk models representing the drag effects induced by the tower [8,9]. Hansen and Pederson [9] have pursued such a combined approach by modeling the effect of the lattice tower by volume forces acting on the three main cylindrical tubes and the smaller connecting tubes and verifying that the momentum deficit of the air equals the specified total force on the tower section. The general findings of such simulations are similar for both tower types, but differ in some specific aspects. One example is the angular position, where the least flow distortion is observed which is about 45° with respect to the wind direction in the case of tubular towers, but almost 90° for lattice towers [8]. In case a fairly unidirectional wind flow pattern exists at the measurement site, these angular positions may be the recommended ones, as opposed to the commonly chosen position where the anemometers face the prevailing wind. Evidently, the effect of flow distortion is a function of the

distance, so that tower effects can be minimized if mounting booms with suitable lengths are used. If the case of the upwind placement of the anemometer is considered, expressions can be derived in order to design the mounting boom for a given type of tower. In the case of lattice towers, the following empirical relationship, based on combined Navier-Stokes/actuator disk model [9] results, has been proposed for the center-line upwind velocity deficit [8]:

$$\Delta = (0.126C_T - 0.006) \left(\frac{L}{R} - 0.08 \right) \quad (32)$$

where C_T is the drag coefficient (dependent on both construction type and porosity of the towers), L is the horizontal tower face width, and R is the distance from the geometrical center of the tower. Expressions for C_T can be obtained from national building codes, such as the Danish wind loading code [8], where the following expression has been proposed:

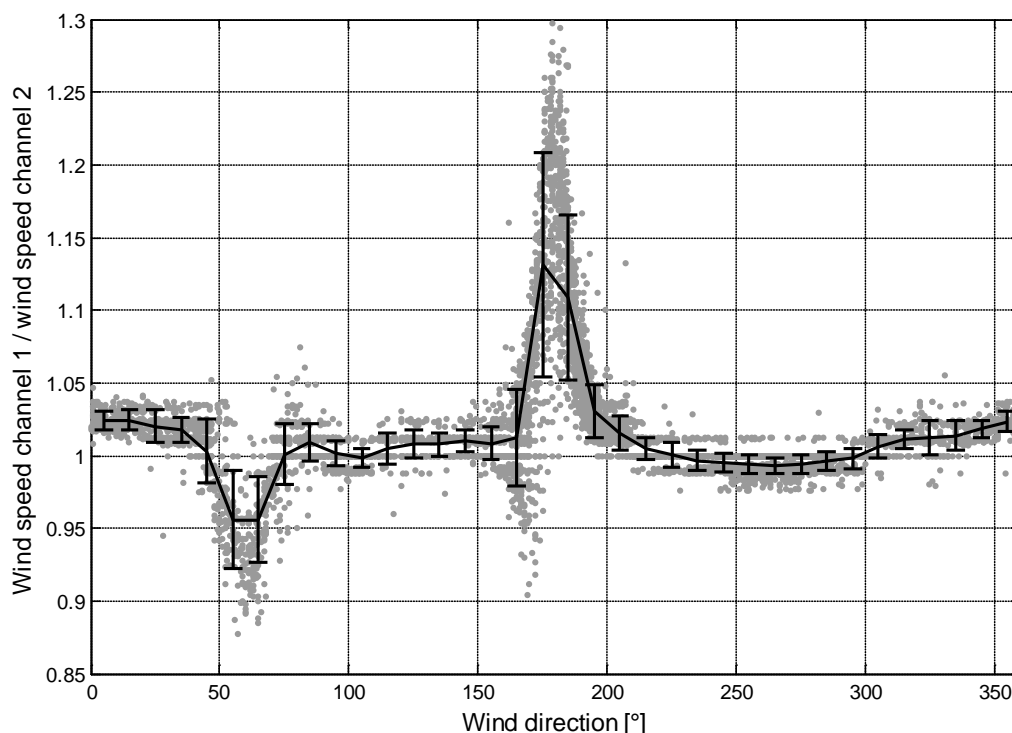
$$C_T = f_{\text{geo}}(1 - p)p \quad (33)$$

where p is the porosity defined by the ratio of the projected area of all structural elements and the overall exposed area and f_{geo} is a drag factor taken as 4.4 for towers with square plane sections and sharp edges, 2.6 for square towers with round edges and 2.1 for triangular towers with round edges. Considering a conservative (high) value of $C_T = 0.6$ and also a conservative value of $L/R = 0.2$ (*i.e.*, corresponding to a boom length five times the face width of the tower) an upwind center-line velocity deficit of about 1.2% is obtained.

Tubular towers, not unexpectedly, show higher velocity deficits at typical distances and do not display a linear behavior as a function of the corresponding distance parameters, taken in this case as d/R , where d is the tower diameter. For a value of $C_T = 0.6$ (calculated in this case directly from the Navier-Stokes equations) and a normalized inverse distance of $d/R = 0.2$ a velocity deficit of 1.6% is obtained.

In situations where the anemometer is directly in the wake of the measurement tower, a major impact on wind speed readings is almost inevitable, since the wake typically extends 10–20 diameters downstream making a mounting of the anemometer at a safe distance difficult. Fortunately, the wake is normally confined to a small angular range so that most readings are not affected by tower shading, especially at sites where a more or less well defined prevailing wind direction exists. CFD simulations [8] indicate that the wake behind a lattice tower has a width comparable to the face width L introduced earlier, whereas, in the case of a tubular tower, the wake width is of the order of three tower diameters for distances greater than about three tower diameters. As a consequence, for mountings with relatively short booms (say, $L/R = d/R = 0.2$), the CFD simulations predict a full width of the angular sector affected by tower shading effects of the order of 10° in the case of lattice towers and about 30° for tubular towers. If the length of the mounting boom is doubled ($L/R = d/R = 0.1$) the full width of the affected angular sector is now about 6° for lattice towers and 17° for tubular towers.

Figure 9. Ratio of wind speed readings recorded by a pair of anemometers mounted on a lattice tower. The continuous line represents bin-averages for a bin width of 10° . Error bars correspond to \pm one standard deviation.



As a consequence, it is a common practice to use two anemometers at a given height above ground level and compare their readings as a function of wind direction. To reduce costs, this analysis is often limited to the highest anemometer level, typically at 60 m. The first or main anemometer should be oriented in such a way that wake effects are avoided most of the time. The limited fraction of the total measurement time during which the main anemometer does suffer from tower shading effects can then be replaced by the second anemometer readings which at that time should be unaffected by wake losses.

An example of tower wake effects is shown in Figure 9 where the ratio of the wind speed readings of two anemometers mounted at 80 m above ground level has been plotted as a function of the readings of the wind direction sensor. The main sensor (channel 1) has been mounted at 240° with respect to true north, whereas the second or redundant anemometer (channel 2) is at 0° . Clearly, the wind speed ratio reflects substantially higher readings of the main sensor at 180° (when the redundant anemometer is in the tower wake) and lower values at 60° (when the main wind speed sensor is in the wake). It can be seen from the figure that tower effects are not necessarily symmetric and reflect to some extent the characteristics of the wind pattern at the site. In the present case, the prevailing wind is from the south, so that the two peaks in the figure have very different associated statistics. Moreover, it should be noted that the angular width of the wake zone is greater than expected from the Navier-Stokes/actuator disk modeling with two angular sectors of 10° width affected at both wind directions showing wake effects. This is not completely unexpected since the CFD model given in [8] only considers a head-on interaction with the actuator disk and angular variations of the effective drag coefficient (as caused by a

variation in the apparent porosity of the lattice structure as a function of wind direction) are not accounted for.

3. Wind Shear

3.1. General aspects

As stated earlier, wind turbines reach quite substantially into the atmospheric boundary layer, with hub heights in the range of 60 to 100 m and blade lengths of up to 50 m. In order to properly assess both the power extracted by the wind turbine (requiring the knowledge of the wind speed at hub height) and the mechanical stresses experienced by the rotor blades (requiring the knowledge of the variation of wind speed over the rotor diameter), a model is needed to predict the full variation of wind speed and related parameters such as relative turbine intensity from a point measurement, generally obtained below hub height. Modern remote sensing techniques like SODAR or LIDAR are a promising alternative to overcome this limitation, but are also subject to several restrictions such as background noise (in the case of SODAR) and averaging volumes.

From boundary layer theory, it is generally assumed that wind speed varies with height according to the prediction of the Monin-Obukhov similarity theory [33-35]:

$$v(z) = \frac{u^*}{\kappa} \left\{ \ln\left(\frac{z}{z_0}\right) - \psi_m\left(\frac{z}{L}\right) \right\} \quad (34)$$

where u^* is the site-dependent friction velocity, z_0 the local roughness length, κ the van Karman constant (usually taken as 0.4) and $\psi_m(z/L)$ the stability function accounting for different thermal conditions of the atmosphere known as stable, unstable and neutral. L is the so-called (Monin-) Obukhov length defined by [35]

$$L = -\frac{u_*^3 T_v}{kgQ_v} \quad (35)$$

where T_v is the virtual temperature defined as

$$T_v = T \frac{1 + r_v/\varepsilon}{1 + r_v} \quad (36)$$

where r_v is the mixing ratio and $\varepsilon (=0.622)$ the ratio of the gas constants of air and water vapor and Q_v the vertical heat flux. The stability function distinguishes between three stability regimes known as stable, unstable and neutral. Under neutral conditions the vertical heat flux vanishes and the stability function is zero (adiabatic case). In this case the vertical wind speed profile in the surface boundary layer becomes logarithmic. If a net upward heat flux occurs, then the Obukhov length is negative and the surface boundary layer is dominated by convection, giving rise to unstable conditions. Convection arises either as a consequence of the absorption of solar radiation by the ground or the advection of cold air over a warm surface; in both cases the result is an increased temperature lapse rate which drives convection. Stable conditions arise when the temperature decreases less with height than in the adiabatic case or even increases (in case of an inversion).

3.2. Assessment of roughness length under neutral conditions

In the practice of wind resource assessment, the effects of atmospheric stability are not always considered, either because the necessary additional instrumentation is not available or because of time constraints of the project development. In case only average values of wind speed and power density over relatively long observation periods (e.g., months) are required, the assumption of an average heat flow of zero can be made and the stability function vanishes. The vertical wind shear then becomes logarithmic and the roughness length can be determined either from a fit to the measured wind speed averages at different heights or from a comparison of the wind speed averages at two different heights. Normally, the fitting technique will provide a more accurate estimate of the roughness length. Occasionally, the inclusion of additional data points may actually diminish the accuracy of the prediction. For example when additional wind speed readings at lower heights which may be affected by vegetation canopy effects and alter the strictly logarithmic dependence. For the discussion of the accuracy of the method and its impact on the extrapolation to greater heights, however, it is sufficient to consider the two-heights method. It is easy to show that the natural logarithm of the roughness length can be written as

$$\ln(z_0) = \frac{v_2 \ln(z_1) - v_1 \ln(z_2)}{v_2 - v_1} = \frac{\delta \ln(z_1) - \ln(z_2)}{\delta - 1} \quad (37)$$

where v_1 and v_2 are the average wind speed readings at the two heights z_1 and z_2 above ground level, and the wind speed ratio $\delta = v_2/v_1$ has been introduced. It is clear from a quick inspection of the formula that the result for $\ln(z_0)$ will depend strongly on δ , given the fact that $\delta - 1$ is generally a small number. After some algebra it can be shown that the standard error for $\ln(z_0)$ can be expressed as

$$\sigma_{\ln(z_0)} = \frac{\gamma_{12}}{(1 - \gamma_{12})^2} \ln\left(\frac{z_2}{z_1}\right) \sqrt{r_1^2 + r_2^2 - 2\rho_{12}r_1r_2} \quad (38)$$

where γ_{12} is the theoretical wind speed ratio derived from the true roughness length $z_{0,\text{true}}$

$$\gamma_{12} = \frac{\ln(z_2/z_{0,\text{true}})}{\ln(z_1/z_{0,\text{true}})} \quad (39)$$

r_1 and r_2 the relative errors of the wind speed measurements at the two heights, and ρ_{12} the correlation coefficient between the two sets of measurements. $z_{0,\text{true}}$ is of course not known a priori and is approximated by the value obtained from equation (37). For ideally correlated wind speed time series ($\rho_{12} = 1$) at the two heights z_1 and z_2 and equal measurement errors ($r_1 = r_2$) the square root in Equation (38) vanishes and therefore the standard error for $\ln(z_0)$. In practice, due to the three-dimensional structure of the wind field and the effect of the tower and booms, the correlation is not perfect, however, ρ_{12} values in the range of 0.990 to 0.995 are typical for differences in measurement height of 20 m. Anemometer uncertainties for individually calibrated instruments are of the order of 0.7%; uncertainties associated to tower wake effects are generally of the order of 0.1% and are therefore negligible compared to calibration uncertainties. From Figure 10 it can be seen how the relative error of $\ln(z_0)$ varies as a function of $\ln(z_0)$ for two different assumptions for the anemometer uncertainty (0.7% and 1.4%, respectively) and two values of the correlation coefficient ρ_{12} (0.990

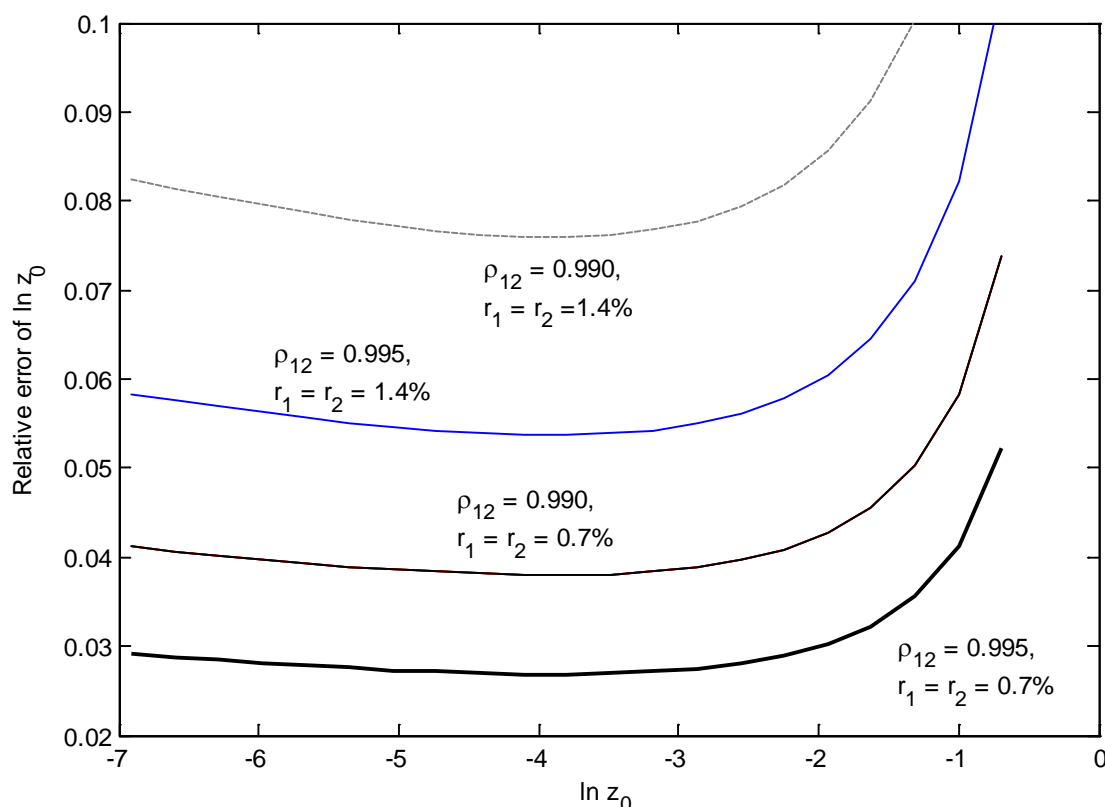
and 0.995, respectively). It is conspicuous that for a high degree of correlation ($\rho_{12} = 0.995$) and an uncertainty representative of a calibrated anemometer (0.7%) the relative uncertainty of $\ln(z_0)$ is of the order of 3%, except for rough terrain ($z_0 \sim 0.5$ m) where $\sigma_{\ln(z_0)}/\ln(z_0)$ rises to about 5%. If uncalibrated anemometers are used and a lesser degree of correlation exists between the wind speed time series at the two heights used for extrapolation, then the relative error of $\ln(z_0)$ can be of the order of 10%, especially for rough terrain. The uncertainty in the logarithmic roughness length translates into a corresponding uncertainty for the ratio γ_{23} of the wind speeds at the hub height z_3 and z_2 :

$$\sigma_{\gamma_{23}} = \frac{\gamma_{23}(\gamma_{23} - 1)}{\ln z_3/z_0} \frac{\gamma_{12}}{(1 - \gamma_{12})^2} \ln\left(\frac{z_2}{z_1}\right) \sqrt{r_1^2 + r_2^2 - 2\rho_{12}r_1r_2} \tag{40}$$

where

$$\gamma_{23} = \frac{v(z_3)}{v(z_2)} \tag{41}$$

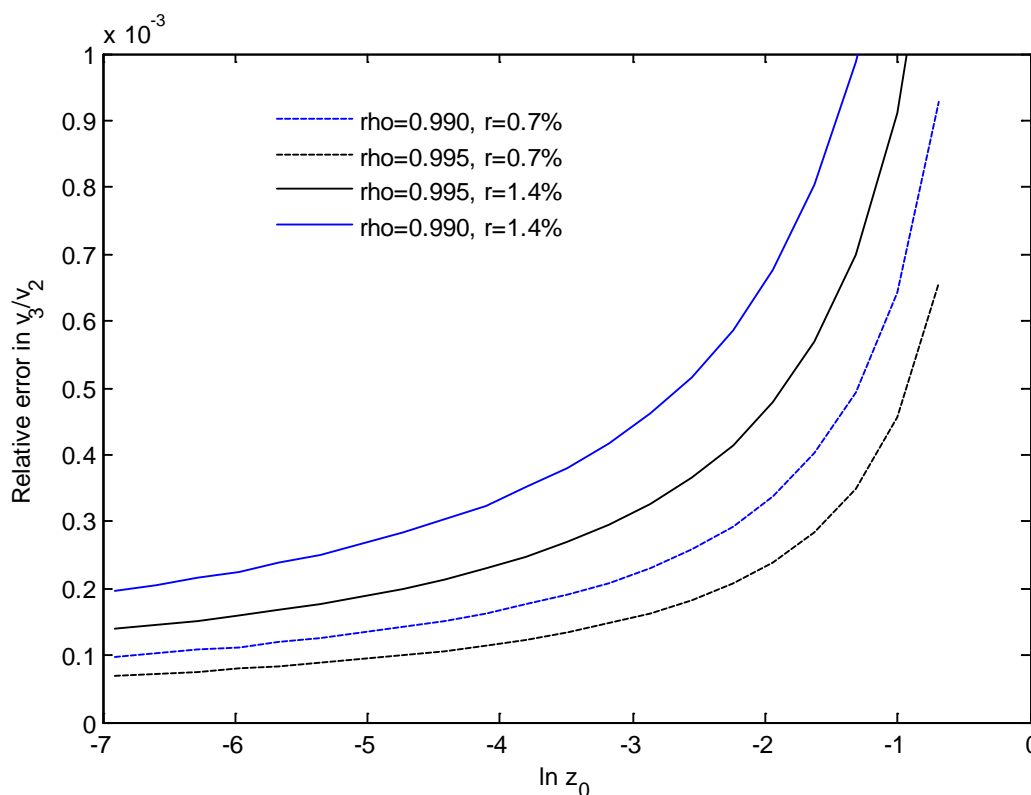
Figure 10. Relative error of the natural logarithm of the roughness length as a function of the natural logarithm of the true roughness length for different anemometer uncertainties and correlation coefficients.



As evidenced by Figure 11, the relative error for the prediction of the hub height wind speed is far smaller than the relative error of $\ln z_0$, covering a range of about 10^{-4} to 2×10^{-3} , depending on the specific assumptions. While $\sigma_{\ln(z_0)}/\ln(z_0)$ is approximately constant over many orders of magnitude, with an increase only for high values of the roughness length, the relative error of γ_{23} increases monotonically with roughness. Even then, it remains at very small values for all parameter values

studied. It should be mentioned, however, that while statistical errors have a relatively small impact on the wind speed prediction at hub height, systematic errors such as those caused by tower wake effects described above may lead to more severe errors in the prediction of wind speed at greater heights, so great care should be exercised when designing and installing sensors on a tower.

Figure 11. Relative error of the wind speed ratio $\gamma_{23} = v(z_3)/v(z_2)$ for $z_2 = 60$ m and $z_3 = 80$ m as a function of the logarithmic roughness length.



In the previous discussion it was assumed that the ground level serves as a reference for the modeling of vertical wind speed profiles. When significant vegetation is present, however, then a systematic vertical shift of the atmospheric boundary layer occurs and the wind speed height dependence can be described by

$$v(z) = \frac{u^*}{\kappa} \ln\left(\frac{z-d}{z_0}\right) \tag{42}$$

with the displacement height d . It has been pointed out [36] that the roughness parameters should not be based on observations below the blending height z^* , defined as the height above the ground where the momentum flux becomes one-dimensional and the average flow no longer varies with the horizontal location [36]. A minimal estimate of z^* is $1.5H$, where H is the typical obstacle height or roughness height; for very low roughness lengths z^* can be estimated by $20z_0$.

From the discussion of statistical errors influencing the determination of the roughness length it is clear that only order-of-magnitude values of the roughness length can be obtained from a measurement of the vertical wind speed profile. This fact has long been taken into account by the creation of roughness classes that characterize the roughness of a given terrain. This approach was pioneered by Davenport and refined by Wieringa [38-40] based on carefully selected experimental results for

homogeneous terrain. Table 1 is an updated version of the Wieringa roughness classes [36], providing the ranges of roughness length z_0 , roughness height H , displacement height d and blending height z^* for a series of homogeneous terrain types.

An important consideration refers to turbulence intensity. As used extensively by Wieringa in his classification of terrain roughness, the mean turbulence intensity can be expressed by [40]

$$\sigma/U = \kappa A / \ln(z/z_0) \tag{43}$$

where U is the mean wind speed and A is the turbulence ratio

$$A = \sigma/u^* \tag{44}$$

The roughness length z_0 can therefore be determined from the observations of the turbulence intensity. It should be noticed, however, that often isolated surface obstacles such as trees, buildings and small hills that are large enough to create considerable wake turbulence, are present in the upwind fetch. If the distance between the obstacles is large enough (greater than about 15 times the obstacle height), the mean wind speed adapts quickly to the local terrain between the large roughness elements. However, the local value of z_0 obtained from these wind speed profiles should not be used to obtain the turbulence intensities because the large-scale wake turbulence created by these obstacles is quite persistent and takes a much longer distance to adapt to the local terrain [36]. The equivalent roughness length values $z_{0,equiv}$ to be used in this case for the determination of turbulence intensity are given in Table 2.

Table 1. Roughness parameters for homogeneous terrain classes [36].

Surface type	z_0 (cm)	H (cm)	d (cm)	z^* (cm) ($20z_0$)
Sea, loose sand and snow	0.02 (U-dep.)	-	-	-
Concrete, flat desert, tidal flat	0.02-0.05	-	-	0.4-1.0
Flat snow field	0.01-0.07	-	-	0.2-1.4
Rough ice field	0.1-1.2	-	-	2.0-2.4
Fallow ground	0.1-0.4	-	-	2.0-8.0
Short grass and moss	0.8-3.0	2.5-5.0	1.3-3.5	16-60
Surface type	z_0 (cm)	H (cm)	d (cm)	z^* (cm) ($1.5H$)
Long grass, and heather	0.02-0.06	0.03-0.06	0.1-0.3	0.05-0.09
Low mature agricultural crops	0.04-0.09	0.3-1.05	0.2-0.9	0.45-1.6
High mature agricultural crops (grain)	0.12-0.18	1.0-2.6	0.6-1.5	1.5-3.9
Continuous bush land	0.35-0.45	2.3-3.0	1.8-2.4	3.45-4.5
Mature pine forest	0.8-1.6	10.0-27.0	10.0-17.0	15.0-40.5
Tropical forest	1.7-2.3	20.0-35.0	27.0-31.0	30.0-52.5
Dense low buildings (suburb)	0.4-0.7	5.0-8.0	3.5-5.6	7.5-12.0
Regular-built large town	0.7-1.5	10.0-20.0	7.0-14.0	15.0-30.0

Table 2. Roughness parameters for heterogeneous terrain classes [36].

Surface type	$z_{0, \text{equ}}$ (cm)	H (cm)	d (cm)	z^* (cm) (1.5H)
Many fields ~200 m wide, separated by thin porous hedges	0.09	4	0.5	6
Sparse bush area (~500 m radius) surrounded by fallow savanna	0.17	2.3	0.9	3.5
Pasture and some narrow woods	0.25	20	7	30
Some narrow woods in open fields	0.3–0.4	10	5	15
Scrawny 1.5 m wide trees on savanna (~20 m spacing)	0.4	8	5	12
Tiger bushes ~20 m wide with ~50 m bare interspaces	0.5	3	2	4.5
Regular bush land	0.43	2.3	1.8	3.5
Woods and some pasture fields	0.85	20	12	30
Scrawny 2 m wide trees on savanna (~10 m spacing)	0.9	9.5	7	15
Woods with some large clearings	1.3	10	5	15
Broken forest	1.2	20	6	30

3.3. The effects of atmospheric stability

Different formulations for the stability function have been published. A common expression is [33]:

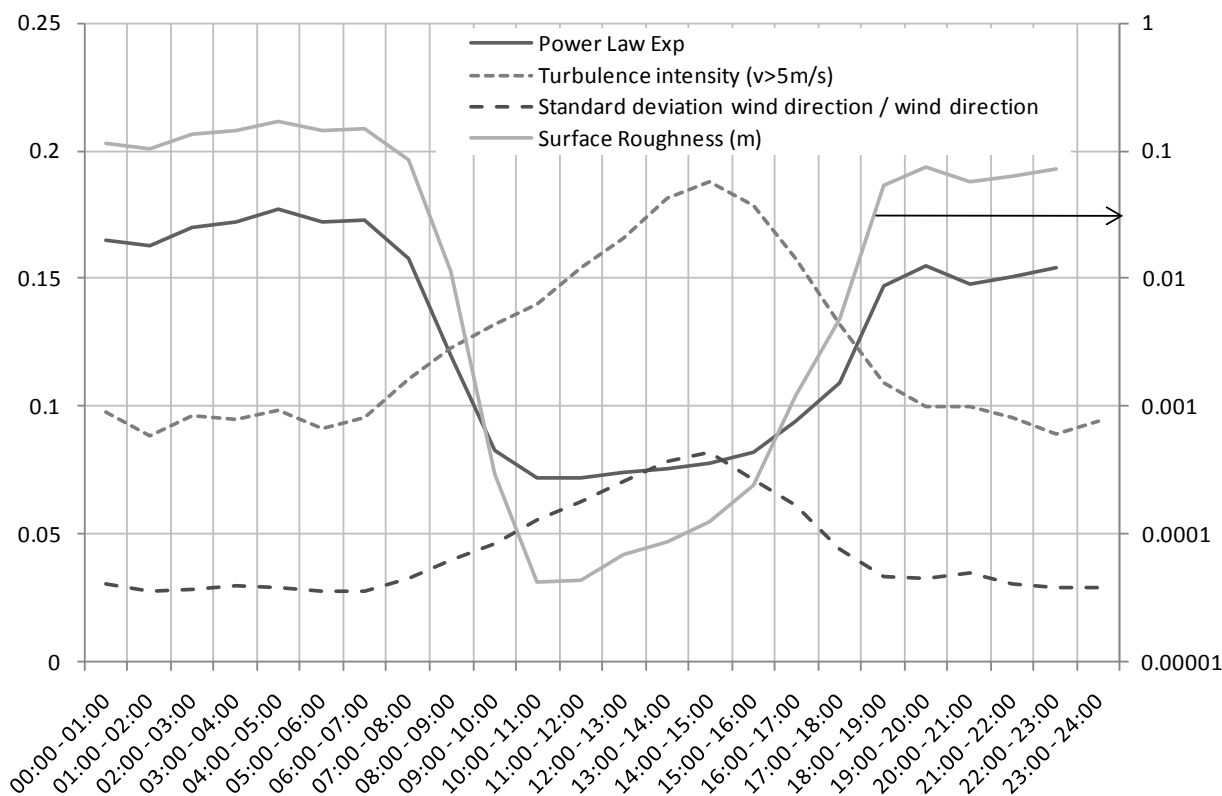
$$\psi_m = \begin{cases} 2 \ln \left(\frac{1 + \phi_m^2}{2} \right) - 2 \arctan(\phi_m) + \frac{\pi}{2} & \text{for } z/L < 0 \\ -\beta \frac{z}{L} & \text{for } z/L > 0 \end{cases} \quad (45)$$

where $\phi_m = (1 - \gamma z/L)^{1/4}$, $\beta = 4.8$, and $\gamma = 19.3$. In the neutral case $\psi_m(z/L) = 0$. It should be noted, that the departure from the logarithmic profile is generally small and a fit of equation (42) to the measured wind speed data is unlikely to provide the correct value of the Obukhov length, unless a range of vertical wind speed values, such as from SODAR measurements, is available. In the common wind resource assessment practice, however, measurements are performed at a few discrete heights (typically 40 m, 50 m, and 60 m) and the measured wind speed values generally adjust well to a logarithmic profile of the form

$$v(z, t) = \frac{u^*}{\kappa} \ln \left(\frac{z}{z_{0, \text{eff}}(t)} \right) \quad (46)$$

where $z_{0, \text{eff}}$ is an effective roughness length, incorporating the effects of both surface roughness and atmospheric stability. As shown in Figure 12 where the values of the apparent roughness or equivalently, the exponents α of a power-law fit of the form $v(z) = Cz^\alpha$ with a constant C have been plotted for a sample case, $z_{0, \text{eff}}$ generally shows a pronounced daily profile, corresponding to the variation from stable stratification during nighttime hours (corresponding to high effective roughness lengths) and very low values during daytime hours when convection and the corresponding vertical momentum transfer drastically reduces the wind shear at typical measurement heights.

Figure 12. Daily variation of apparent surface roughness for a six-month measurement period compared to the corresponding variation in relative turbulence intensity and fluctuations in wind direction.



In order to illustrate the effect of atmospheric stability on the effective or apparent roughness length we have used Equation (46) to calculate $z_{0,eff}$ from measurements of the wind speed at typical monitoring heights of 40 m, 50 m, and 60 m for a range of values of the true roughness length z_0 . The results have been plotted in Figure 13.

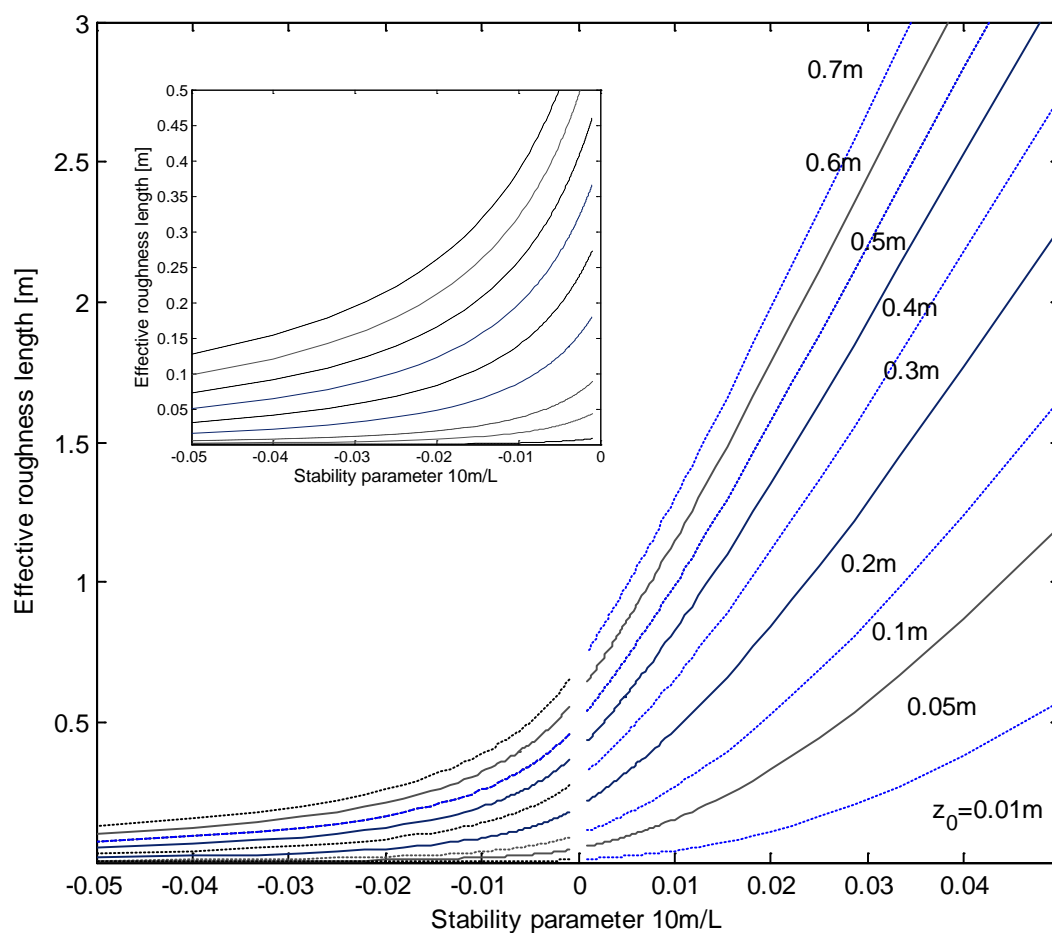
It is evident from Figure 13 that the effective roughness length varies substantially with the stability parameter $10 m/L$, so that an extrapolation to greater heights using a constant (average) roughness height may introduce significant errors, especially if the hourly profile is of interest. Referring again to Figure 11 we observe that in this case $z_{0,eff}$ equals 0.1m during evening and nighttime hours and drops to about 10^{-4} m during the daytime hours, with the transition occurring in about two hours during the morning and some three hours in the evening. As evidenced by the graphs for turbulence intensity $TI (= \sigma_v / \bar{v})$ and a corresponding measure for the variation of the wind direction $(= \sigma_\theta / \bar{\theta})$, this reduction in apparent roughness is a direct consequence of the onset of convection during the morning hours, triggered by the absorption of sunlight on the ground. Clearly, the use of an average roughness length to extrapolate the wind speed readings to hub height would under-predict the hub height wind speed during nighttime hours and over-predict it during the daytime. If the wind speed measurements are conducted at 40 m, 50 m and 60 m and the turbine hub height is 80 m, then sufficient accuracy may be obtained if extrapolation is performed for each time step t_i using the effective roughness length $z_{0,eff}(t_i)$. If the gap to be bridged by the extrapolation is higher, it may be advisable to determine the

Monin-Obukhov length L at every time step for a more accurate prediction of hub height wind speed. The vertical heat flux required for the determination of L can be calculated from

$$Q_v = \langle \rho C_p w'T' \rangle \tag{47}$$

where w' and T' are the fluctuations of the vertical wind speed and the temperature around their average values, ρ is the air density and C_p the specific heat of air. The measurement of Q_v requires an anemometer with a short length constant and a data logger capable of calculating the instantaneous product $w'T'$ before averaging.

Figure 13. Effective or apparent roughness length as a function of the stability parameter $10\text{ m}/L$ for different values of the true roughness length, both under stable and unstable conditions. *Inset:* Magnified portion of the negative range of $10\text{ m}/L$ (unstable stratification).



An alternative lies with the measurement of the solar radiation which has been related to the mean vertical heat flux by some authors. Koo *et al.* [41] propose to calculate Q_v from

$$Q_v = \begin{cases} 0.4(G - G_0) & G \geq G_0 \\ 0.4(1 - n/8)(G - G_0) & G < G_0 \end{cases} \tag{48}$$

where n is the cloud cover in oktas ($0 \leq n \leq 1$), G is the total solar radiation measured in the horizontal plane and $G_0 = 100\text{W}/\text{m}^2$. Evidently, Equation (48) represents a gross oversimplification of the problem, so care has to be taken before using this approach for vertical extrapolation.

Other alternatives for determining the wind speed at hub height and/or over the rotor diameter include the use of vertical profilers such as SODAR and LIDAR as mentioned before, and of course, tall towers, though the steep rise in cost with increasing height puts a limit to the number of hub height towers that can be deployed at a potential development site, at least during the early development.

4. Long-Term Assessment and MCP (Measure-Correlate-Predict) Methods

4.1. General approach

Since typical wind farm assessments last anywhere from one to three years, with important decisions to be taken often only after several months, there is an obvious need for a prediction of the performance of a planned wind farm during its expected life time (20 years or more). Such an assessment is an important part of the wind farm financing process. While the measurement campaign may correspond to an untypically high or low period, correlations with nearby reference stations should help detect such trends and provide a corrected long-term estimate of the wind speed at the development site and its interannual variations. Moreover, since the power output of wind turbine depends on the wind speed in a non-linear way, the distribution of the wind speed values should also be predicted correctly.

The general approach is to look for a relationship between the wind speed variables v_{site} and v_{met} of the site under development and a suitable reference station, respectively [42-45]:

$$\hat{v}_{\text{site}} = g(v_{\text{met}}) \quad (49)$$

where \hat{v}_{site} refers to the predicted wind speed at the site. Since the correlation period is necessarily limited, one basic assumption is that equation (49) correctly describes the long-term relationship between the two variables. The wind resource at either site, on the other hand, fluctuates over the years. The objective of the procedure is now to determine the long-term wind speed distribution function $f_{\text{site,long}}(v_{\text{site}})$ from the knowledge of the corresponding distribution at the reference site. Due to the conservation of probability we have

$$f_{\text{site,long}}(\hat{v}_{\text{site}})d\hat{v}_{\text{site}} = f_{\text{met,long}}(v_{\text{met}})dv_{\text{met}} \quad (50)$$

and therefore

$$f_{\text{site,long}}(\hat{v}_{\text{site}}) = f_{\text{met,long}}(g^{-1}(\hat{v}_{\text{site}})) \frac{1}{dg/dv_{\text{met}}} \quad (51)$$

where we have assumed that the relationship (49) can be inverted.

4.2. Linear methods

Often, it may be suitable to consider several reference stations with concurrent data sets for a given development site; equation (49) has then to be generalized to

$$\hat{v}_{\text{site}} = h\left(v_{\text{met}}^{(1)}, v_{\text{met}}^{(2)}, \dots, v_{\text{met}}^{(n)}\right) \quad (52)$$

Often, a linear relationship of the form

$$\hat{v}_{\text{site}} = a_0 + a_1 v_{\text{met}}^{(1)} + a_2 v_{\text{met}}^{(2)} + \dots + a_n v_{\text{met}}^{(n)} \quad (53)$$

is assumed between the wind speed variables; standard (multiple) linear regression techniques can then be used, providing useful descriptive statistics including p -values, variance inflation ratios (VIR), a R^2 -value and standard errors for each of the fit parameters and the predicted wind speed. While the standard statistical tests for significance and the calculated standard error provide a useful first estimate, a low standard error is no guarantee for an accurate prediction of the long term wind resource (as characterized by mean wind speed, mean wind power density, wind speed distribution and related parameters), since the fit parameters in Equation (53) may change over time, responding to intra- and inter-annual variations of the regional wind flow pattern.

Wind speed time series can be analyzed irrespective of wind direction; generally, however, wind direction is binned into a certain number of sectors and the wind speed subsets for each direction bin are analyzed separately for their correlation. Since wind direction readings may not always coincide, binning may be based either on the wind direction measured at the reference station(s) or the development site. If the differences between the wind direction readings at the reference and the measurement sites are too substantial, then different approaches may be taken. When a systematic veer occurs (e.g., in response to a bend in topography), the relationship between the site and the met direction may be fitted to a polynomial and the fit curve may be used to predict the long-term site wind direction. A more general approach was put forward by Woods and Watson [45]; the authors propose to first bin all concurrent wind direction data for both sites into a matrix, then reject matrix values with low occurrence values (typically <5%) and then define a filtered concurrency matrix Z_{ij} running over site direction indices i and met direction indices j and subjected to the condition $\sum_j Z_{ij} = 1$. The sectorized site wind speed data are then correlated with the met data by either

$$\hat{v}_j^{(\text{site})} = \sum_{i=1}^N Z_{ij} (m_i v_i^{(\text{met})} + c_i) \quad (54)$$

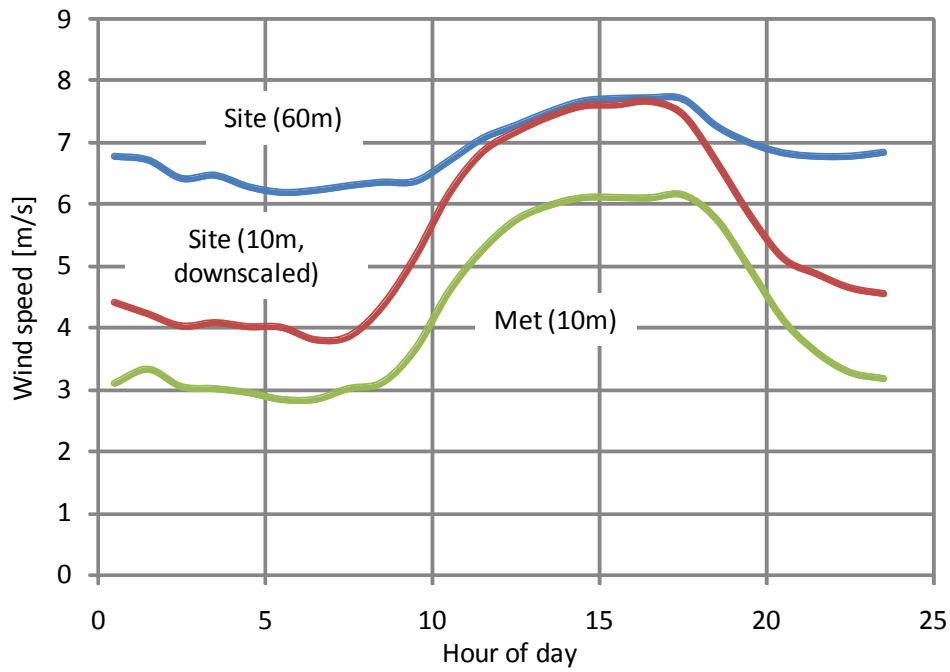
or

$$v_j^{(\text{site})} = m_j \sum_{i=1}^N Z_{ij} v_i^{(\text{met})} + c_j \quad (55)$$

where (m_i, c_i) are the linear fit parameters obtained for concurrent wind speed data in the angular sector i . In the first approach, the sectorized regression relationships contributing to a given site wind direction sector j are weight-averaged, while in the second one, the met wind speeds themselves are averaged before applying the sector regression relation for the site wind direction sensor j . The authors state that the second approach yields better back-prediction results for their cases. They then go on to demonstrate their method for one site pair with 100 observation days and a pronounced “channeling” effect, *i.e.*, data showing a systematic veer between the bearings of met and site towers. While the overall predicted wind speed was found to be almost identical for a standard linear regression, a veer-correcting MCP technique and the matrix-averaging method proposed by the authors, the angular average wind speeds were found to be better predicted by the new method. No details on the intervals used for obtaining the sectorized linear fit parameters and the back-prediction period were given

however, and the authors recognize that the concurrency period for the one period studied was too short to make statements about the performance of the method under intra- or inter-annual fluctuations.

Figure 14. Daily profiles for a prospective at 60 m height above ground and downscaled to 10 m using hourly wind shear coefficients, as well as the 10 m met station profile.



While average value of the wind speed is generally the most important individual parameter, the effect of the fluctuations around the mean as measured by the standard deviation of the hourly values in a given period and the wind speed distribution parameters (often taken as the scale and shape factor of a Weibull distribution) is important for the determination of wind power density and, ultimately, turbine yield. From an inspection of equation (53) for the case of a two-site relationship it becomes clear immediately that the simple linear regression method runs into problems when it comes to predicting fluctuations. From equation (53) with $a_0 = b$ and $a_1 = m$ we have

$$\hat{\sigma}_v^{(site)} = m\sigma_v^{(met)} = \left(\alpha - \frac{b}{\langle v_{met} \rangle} \right) \sigma_v^{(met)} \tag{56}$$

where

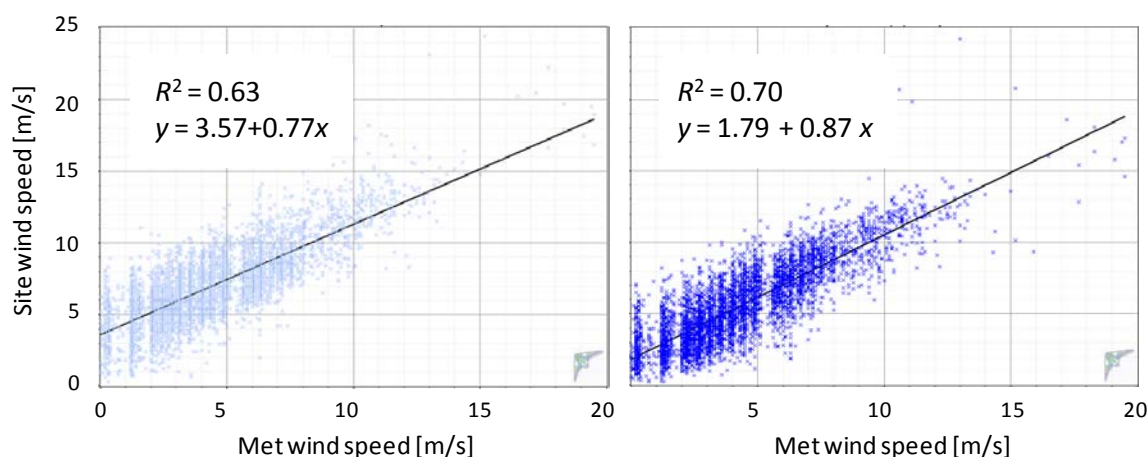
$$\alpha = \frac{\langle v_{site} \rangle}{\langle v_{met} \rangle} \tag{57}$$

is the ratio of the average wind speeds at the prospective and the met site, respectively. Equation (56) illustrates several of the shortcomings of the standard linear regression approach: (1) First, the standard deviation of the predicted wind speed is fixed by the linear fit parameters and cannot be specified independently. (2) For zero intercept ($b = 0$) the standard linear regression predicts that the standard deviations scale as the mean wind speeds, which may be acceptable for power prediction purposes; for a finite intercept, however, the predicted standard deviation is strongly influenced by the vertical intercept. In the typical case, the met anemometer is located at a low height (generally 10 m), where the

target site measurements are taken in the range of 40 m to 60 m. The intercept is then generally positive, and the predicted wind speed distribution will be narrower than the distribution measured at the met site. Consequently, the predicted Weibull shape factor will be substantially higher than the typical values measured at the site.

There are several ways of working around this restriction, while still preserving the idea of a linear relationship between prospective site and the met station. One possible approach is to look into possible reasons for high vertical axis intercepts and make the corresponding adjustments. As mentioned above, often measurements from near-surface (10 m) are correlated with near-hub height measurements for a lack of a tall tower reference data. Daily profiles at such different heights vary quite substantially, with surface winds peaking during the early afternoon hours when convection creates an unstable atmospheric boundary layer. Hub height winds, on the other hand, often have their peak during the late afternoon or night hours. Consequently, wind shear is often largest when site winds are high, whereas it is low when site winds are low. When fitting the met/site data to a straight line, this situation leads to a positive site axis intercept which increases with the phase lag. To compensate for this problem, the wind speed at the site (where generally readings at different heights are available) may be downscaled to 10 m before performing the regression analysis. The inferred long-term wind speed data at the site may then be scaled to 60 m again using the detailed measured hourly and seasonal vertical shear obtained at the site. Clearly, it has to be verified on a case-by-case basis that the additional extrapolation step does not make up for the reduction in prediction error obtained by the downscaling.

Figure 15. Regression plots for hourly wind speed values. (a) Correlation of 60 m site data with 10 m met data. (b) Correlation between the downscaled (10 m) site data and the 10 m met data.



In Figure 14 it can be seen how the downscaling process favors the correlation between the site and the met data. While the site wind speed data collected at 60 m vary little with time of day (from about 6.2 m/s to 7.8 m/s), the site wind speed data downscaled to 10 m show a very similar profile to the reference wind speed collected at an airport some 50 km away from the site. Both the virtual anemometer readings and the met station readings show a variation by about a factor of 2 between nighttime and daytime hours and the two curves are almost in phase. It therefore comes as no surprise

that the correlation between the two data sets improves significantly as a result of the downscaling process (Figure 15); whereas the R^2 -value for the original two data sets was 0.63, after downscaling the R^2 -value increased to 0.70. Moreover, the vertical axis intercept decreased significantly from 3.57 to 1.79, resulting in a greatly reduced wind speed distribution narrowing effect.

Rogers *et al.* [44] recognized the importance of correctly predicting the site variance and proposed a simple linear method, termed the variance ratio (VR) method. After reviewing a series of different MCP approaches documented in literature they conducted a systematic assessment of three published methodologies and compared them to the VR technique using five metrics defined by the ratios of the predicted and the measured long-term wind speed and power density, respectively, as well as similar relationships for the Weibull shape and scale factors. In the variance ratio method, the long-term wind speed values are predicted according to the relationship

$$\hat{y} = (\mu_y - (\sigma_y/\sigma_x)\mu_x) + (\sigma_y/\sigma_x)x \quad (58)$$

where μ_x, μ_y, σ_x , and σ_y are the means and standard deviations of the two concurrent data sets, respectively. By construction, the predicted wind speed data set (variable y) has the same mean and standard deviation as the measured data set during the concurrent period. While surprisingly simple, the VR method was found by Rogers *et al.* [44] to provide the most accurate predictions of all metrics analyzed.

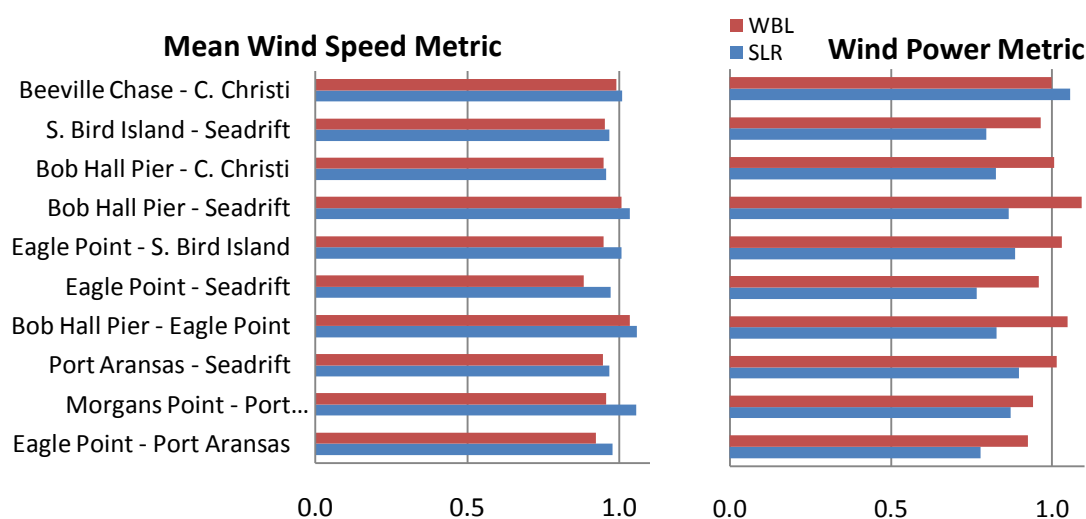
4.2. Non-linear approaches

While linear correlation methods are still favored by many consultants and most commercially available software packages for wind park development rely on such methods, more complex methods have been developed in recent past. One approach, put forward by Romo *et al.* [46], goes beyond ad hoc approaches by recalling that linear regression has its theoretical underpinning in the fact that two linearly correlated data sets can be derived from a joint or bivariate normal distribution function. Such a function, when integrated over one of the wind speed variables, results again in a normal (univariate) distribution function. Hourly wind speed values, however, are not well described by normal distribution and generally follow Weibull distributions. The correct bivariate distribution for a site pair should therefore reduce to Weibull functions when integrated over either of the variables. An obvious choice is a bivariate Weibull distribution function. The authors use this idea to derive a theoretical regression function for a site pair which depends directly on the fitted bivariate distribution parameters; the predicted relationship between the variables is generally non-linear. The authors argue that while there may be little or no improvement as to the prediction of wind speed (by definition, the linear regression predicts the wind speed correctly for the regression time period), the new method may be more suitable for capturing fluctuations of the hourly wind speed and therefore better predict power density and turbine yield.

In Figure 16, the results obtained with this method are shown for 10 pairs of site in the Texas coastal region. Most stations correspond to the Texas Coastal Oceanic Observation Network (TCOON) [47], while the stations Beeville and Corpus Christi are located at airports. The results of the method are expressed as metrics for wind speed and power density defined by the ratio of the predicted and the observed long-term value, and are compared to the corresponding results obtained with a Simple

Linear Regression method (SLR). In both cases, the analysis was performed for sectorized wind speed data; the results reported represent the weighted averages. It is conspicuous from the figure that the accuracy in wind speed prediction is similar for both methods; in the case of the wind power density, however, the new method (termed WBL in Figure 16) provides a significantly improved prediction over the linear method which interpredicted the power density for all cases but one. It is noteworthy that all site pairs studied have a relatively low correlation coefficient; it is believed that precisely in these cases the new method unfolds its potential, whereas in cases with high correlation and low vertical axis intercept linear methods may be appropriate and preferable due to the ease of use.

Figure 16. Mean wind speed and wind power density metrics (=predicted/true wind speed and wind power density, respectively) for the 10 pairs of sites [46].

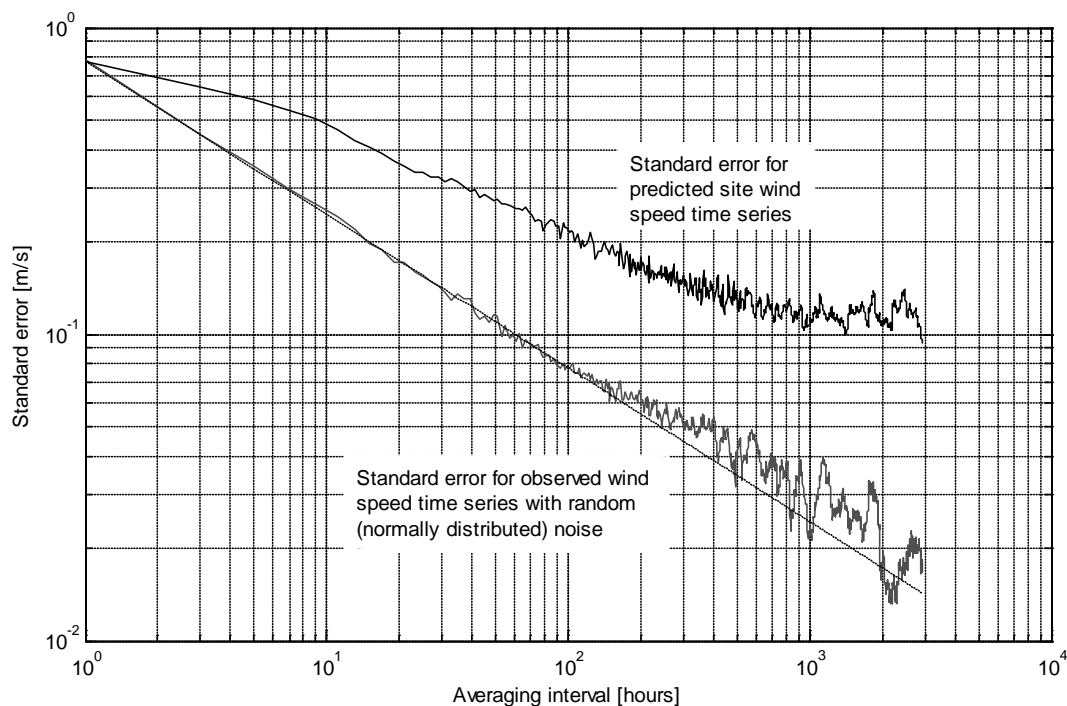


4.3. The choice of reference data

An important point refers to sources for reference data. Often Automated Surface Observation Stations (ASOS), such as the ones located at airports or the ones operated by national weather services, are used as references. While the density of such stations is often not very high, with distances between adjacent stations of the order of 50 to 100 km and quite variable track records ranging from about 5 to 50 years, these stations may often be first choice for an initial inspection of the long-term fluctuation patterns. Other networks may have a limited regional extension, such as the Texas Coastal Oceanic Observation Network (TCOON) [47] in the US or have been installed only recently, such as the Agricultural Climate Observation Network of INIFAP in Mexico and are therefore of limited use for the detection of long-term trends. In any of these cases, wind speed is often not of primary interest to the operators of the observation network, and the relatively low altitude Above Ground Level (AGL) of 10 m used by international conventions is often not representative of the hub height wind speeds required for wind farm yield estimations. Additional sources of information are radiosonde measurements carried out on balloons and satellite measurements. Radiosonde deployment sites are located on a much coarser grid than ASOS stations but contribute valuable information as to the three-dimensional structure of the atmosphere [48]. Satellite measurements, finally, are potentially capable of evaluating wind speed at arbitrary locations but rely on indirect methods such as the

synthetic aperture radar (SAR) [49] and scatterometers. Combining the different sources of information into one consistent picture will be one of the main challenges in the near future.

Figure 17. Evolution of the standard error of an MCP-derived wind speed prediction as a function of the averaging interval compared to the standard error obtained by adding normally distributed noise.



While typically hourly wind speed averages are used for long-term resource assessment studies, other choices are possible. On-site measurement systems are generally configured to store 10-min intervals, based on the standard assumption of wind engineering that there is spectral gap between the short-term turbulent fluctuation with time scales of up to a few minutes and longer-term diurnal and synoptic phenomena with time scales in excess of several hours [50]. If long-term tall tower measurements are available in the project region, then 10-min data would be the obvious choice. ASOS stations, on the other hand, only occasionally provide 10-min data. While for some stations 1-min data are available, often only 2-min averages recorded on top of the hour are provided. Weather modeling data such as those generated with the NAM (North American Mesoscale Model) [51] or reanalysis data produced by NARR (North American Regional Reanalysis) [52] are created in three-hour intervals. Even if shorter-term reference data are available for correlation purposes, additional averaging may be required to obtain higher correlation between the data sets and a low standard regression error. Though a high correlation is not a sufficient condition for an accurate long-term prediction, it is generally a pre-requisite. Clearly, the longer the wind speed averaging interval, the more information is lost which has to be reconstructed afterwards. If daily averages are used, the daily profile has to be reconstructed, e.g., by using the rescaled daily profile obtained from on-site data, in order to generate the 12 (months) \times 24 (hours) wind speed and power production tables generally required by lenders. Monthly values can still be used for global estimates of the long-term production, but then suitable monthly wind speed distributions have to be determined. As opposed to daily values, monthly wind

speed histograms can often be fitted well to Weibull distribution functions, the shape factor of which can then be used for power density and turbine yield calculations. (The scale factor is calculated from the predicted mean wind speed and the assumed value of the shape factor).

The accuracy of the processes described above will depend on the reduction of the regression error upon increasing the averaging interval. This decrease will depend on the time scales of unknown processes that account for a less than perfect correlation between the reference and the prospective site. The functional dependence is site-pair specific, but in our experience power law relationships with an exponent of the order of -0.20 to -0.25 provide good estimates. Figure 17 shows the standard error of a linear regression for two sets of one-year wind speed data, both recorded at 60 m AGL. For comparison, the lower curves shows the standard error of a regression between the reference tower wind speed data and a third data set created from the reference data by adding normally distributed noise with a standard deviation set equal to the standard error the other correlation for hourly values. As expected from standard statistical results, the standard error in the case of the normally distributed noise decreases as the inverse square root of the length of the averaging interval in hours. The standard error in the case of the real site pair, however, decreases much slower, being almost an order of magnitude higher for monthly averages than one would expect from random noise.

5. Extreme Winds

5.1. Types of extreme wind

Wind turbines, like any high-rise structure, are susceptible to high wind events which can potentially compromise the structural integrity of the turbines. An assessment of the extreme winds in the area of interest is therefore generally an integral part of any wind resource study for a planned wind farm. Several main categories of severe storms leading to extreme wind conditions can be distinguished, with hurricanes and tornadoes being the most well-known phenomena, even though by far the majority of all potential wind farms are affected by so-called well-behaved storms, rather than by hurricanes and tornadoes.

Hurricanes emerge from low-pressure centers above the ocean in the tropics and move towards higher altitudes [33]. The mechanism which sustains the hurricane's energy conversion relies on the massive evaporation from the ocean caused by the low pressure in the hurricane and is no longer available at landfall, causing the hurricane to decay in intensity while moving inland. Hurricanes and related phenomena (such as typhoons and cyclones) are therefore restricted to low altitude coastal sites. Tornadoes, on the other hand, are believed to be due to an interaction of a near-surface warm and moist air layer, a dry cool layer, and the high speed jet stream at great altitudes (10–12 km) [33]. The interaction of the jet stream with the dry layer, combined with the ascending moist air produces an evaporatively cooled descending dry air mass which, under appropriate conditions, may evolve into a tornado. Since the jet stream is a quite typical phenomenon of the continental United States, it comes as no surprise that the midwestern states of the US are especially plagued by tornadoes.

While hurricanes and tornadoes are characterized by rotating air masses and are generally not representative of the average wind climate in a given region, other extreme wind events like thunderstorms, straight-line winds, downbursts or mountain downslope winds like the *Foehn* in the

Alps or the *bora* in the former Yugoslavia can often be considered as an extreme condition of the average wind climate. Estimates of the probability of encountering a given extreme wind speed or dynamic pressure value in a given period (often taken to be 50 years) can then be obtained from an extrapolation of the observed wind speed statistics during shorter periods.

5.2. Extreme wind statistics in well-behaved climates

In the following, we will describe the framework for predicting extreme wind speeds under the assumption that normal and extreme wind events can be derived from the same underlying distribution; the kind of climates where this assumption is valid are called *well-behaved*. Regions which are under the influence of hurricane and tornado events have to be treated separately. The reader is referred to texts on wind engineering for a discussion of the corresponding approaches [33,53]. In order to provide a statistical expression for calculating such extreme wind speed values we first define the *exceedance probability* $P_E(v)$ as the probability that the wind speed v will be exceeded during a one-year period. Closely related with P_E is the *return period* T_R defined by [54-56]

$$T_R(v) = \frac{1}{P_E(v)} \quad (59)$$

T_R can be interpreted as the average number of years that have to pass before such an event arises. Note that the definition above applies in principle to any suitable average value of the wind speed, but 10-minute averages $v_{10 \text{ min}}$ (sometimes referred to as sustained wind speeds) and 3-second averages v_{3s} (generally termed gusts) are frequent choices. Electronic data loggers generally record both the 10-minute average and the highest 3s-gust that occurred during the 10-minute averaging interval. Clearly, it is very important to state whether a given return period refers to a sustained wind speed value or a gust, since the gust by definition is higher than the average. Another common choice for a representative averaging interval is the concept of the annual fastest-mile wind speed used in the US. The fastest-mile wind is the peak wind speed averaged over a distance of one mile passing through the anemometer.

A frequent approach to calculate the exceedance probability for a given observation period is to list the highest annual wind speed values (either sustained, gust, or fastest-mile) in a ranked fashion, starting with the highest year (rank $r = 1$) and working down to the lowest year ($r = N$, N being the total number of years in the observation period). P_E is then calculated from [56] (see also [54] for an earlier approach):

$$P_E(v) = \frac{r}{N + 1} \quad (60)$$

Since generally the observation period does not cover the period (typically 50 years) required by wind turbine standards, an extrapolation is required. Such an extrapolation is based on the concept of the cumulative distribution function (CDF) $F(v)$ introduced earlier. Note that the exceedance probability and the CDF are related by

$$P_E(v) = 1 - F(v) \quad (61)$$

Whereas normal winds are often well described by a Weibull distribution, extreme values have been found to follow a so-called Gumbel, type-I or Fisher-Tippert distributions [58]. Gumbel distributions are

actually applicable to many phenomena involving extreme values under quite general assumptions for the parent distribution, *i.e.*, the general distribution from which the extreme values have been extracted.

The Gumbel distribution is given by

$$F(V) = \exp\left(-\exp\left(-\frac{a+V}{b}\right)\right) \quad (62)$$

where

$$\begin{aligned} a &= 0.450 \sigma - \bar{V} \\ b &= 0.780 \sigma \end{aligned} \quad (63)$$

and \bar{V} is the average value and σ is the standard deviation of the extreme value variable V . In order to determine the extreme wind speed for a specified return period T_R one can now plot the inverse of the cumulative distribution function, the so-called percent point function, *vs.* the measured extreme values of the wind speed and obtain the best linear fit to the data. From equation (62) we have

$$\ln(-\ln(1-1/T_R)) = -\frac{a+V}{b} \quad (64)$$

for a given return period T_R , *i.e.*, $\ln(-\ln(1-1/T_R))$ should be a linear function of the extreme wind speed V . Often, the highest yearly wind speed V_{year} is used as the independent variable; T_R is then specified in years. At wind farm development sites, on the other hand, often only short-term records are available. Then, using monthly maximal sustained wind speeds can be used and the return period T_R has to be specified in months.

Figure 18 shows two examples for extreme wind distributions obtained from the largest observed sustained wind speeds at Little Rock, AR, for the period of 1943 to 1977 and Corpus Christi, TX, for 1943 to 1976. The so-called fastest-mile wind speed, defined as the peak wind speed averaged over one mile of wind passing through the anemometer, has been used as the wind speed variable. It can be seen that the values obtained from Little Rock adjust themselves pretty well to a Gumbel type I distribution and 50-year return value typically required for extreme structural load calculations can be predicted reliably. In the case of Corpus Christi, on the other hand, the linear fit is generally poor and more importantly, the distribution does not account for hurricane events such as the 128mph event shown in Figure 18 which is far off the linear trendline. The assessment of extreme winds in hurricane-prone areas requires modifications of the simple theory discussed here. For a detailed account the reader is referred to specialized texts on wind engineering and structural dynamics [33,53].

For spreadsheet calculations it is often convenient to provide an explicit expression for the maximum wind speed in a given return period. Using the approximation $\ln(-\ln(1-1/T_R)) = -\ln T_R$ we can calculate the extreme wind speed corresponding to a return period T_R

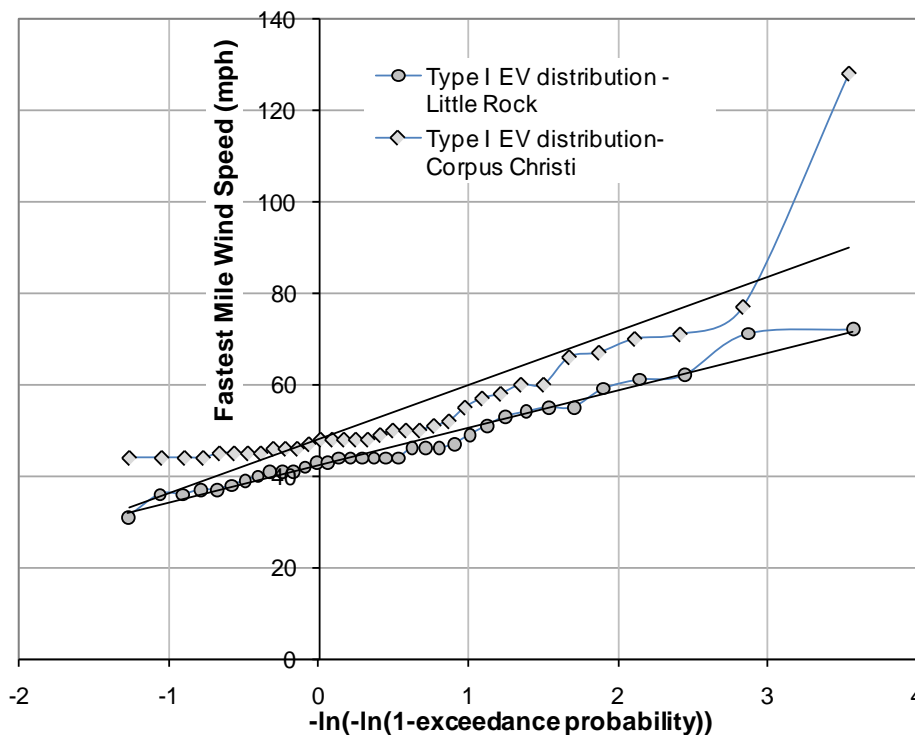
$$V(T_R) = \bar{V} + 0.780 (\ln T_R - 0.577) \sigma \quad (65)$$

where T_R is again in years. Similarly, an expression for the standard deviation of the largest yearly wind speeds within the return period can be calculated [33]

$$SD(V(T_R)) = 0.78 \left[1.64 + 1.46 (\ln T_R - 0.577) + 1.1 (\ln T_R - 0.577)^2 \right]^{1/2} \frac{\sigma}{\sqrt{n}} \quad (66)$$

where n is the sample size. In case monthly values are used, T_R has to be replaced by $12 T_R$ in both formulas. In the former discussion we have implicitly assumed that the extreme wind speed observations are independent, which is a good approximation if annual or monthly values are considered.

Figure 18. Extreme Value Distributions for two sample cases (Little Rock and Corpus Christi).



6. Modeling of wind flow

6.1. General considerations

The generation of maps is essential to many science and engineering disciplines. The general idea is to combine point measurements of a given variable f with a suitable mathematical model which relates the value of the variable at a given location (x, y) with that at a reference location (x_0, y_0) . Given that model, in principle one point measurement is enough to generate a full map $f(x, y)$. In practice, however, at a greater distance from the reference location the model may yield results with little accuracy, so additional measurements at locations (x_i, y_i) may be required. Clearly, if measurements at a great number of locations are available, then no mathematical model may be required and an interpolation between the measurement locations may be sufficient. This situation is typical of geophysical mapping studies, where a series of spatially distributed point measurements are combined into a map by using weighted interpolation techniques like universal Kriging [59].

Point measurements in wind energy assessment, on the other hand, are both costly (>US\$25,000 for a 60 m tower-based measurement system, some US\$50,000 for a corresponding 80 m system) and time-consuming with required measurement periods of at least one year. Therefore, wind mapping studies generally have to rely on mathematical models and few reference points. In principle, the underlying equations for fluid flow are well known. However, due to the complexity of solutions it is necessary to implement a hierarchical approach. If the wind map is required for the micro-siting of turbines mainly, then often the modeling domain has lateral dimensions of the order of 10–20 km and a few measurement towers at the site may adequately represent the local wind climate. The role of the model is now to assess the effect of the local topography and roughness on the local wind climate.

Models for micro-siting can be roughly divided into linearized and full computational fluid dynamics (CFD) models. Both linear and CFD models are nowadays available for purchase. Linearized models like WASP [60] or MS-Micro/3 (implemented, e.g., in the Wind Farm package by ReSoft) [61] have typical execution times of a few minutes on a standard 1GHz/1Gbyte PC for a typical calculation domains of 512×512 points, enough to cover a simulation domain of $25 \text{ km} \times 25 \text{ km}$ at a resolution of 50 m. Full CFD models will require several hours to perform a similar task. Linearized models, on the other hand, will provide useful results only if it can be assured that the flow lines will remain attached to the surface in the complete simulation domain, whereas CFD models can handle situations where flow separation occurs. While standard CFD packages like Fluent or CFX are capable of modeling situations of interest for wind turbine siting, in practice a lot of effort has to be put in the setup of the simulation and the extraction of the results. As a response to this, commercial CFD wind farm simulation tools like WindSim and Meteodyn have become available, providing an environment where the geographical input information (both topography and roughness) can be conveniently combined with the measured wind data, generally termed a *wind rose* or a *climatology*.

Both linear and full CFD maps first generate normalized wind flow maps for each of a user-defined number of wind directions and then combine these maps with the measured wind rose at one or several locations to obtain maps for the average wind speed, wind direction, wind power density, and turbine yield. Full CFD models are also capable of predicting additional parameters like turbulent kinetic energy.

6.2. Linearized models

One particular model, the MS-Micro/3 or MS3DJH model, is based on the theory developed originally by Jackson and Hunt and by Mason and Sykes and extended and developed by Walmsley *et al.* [62,63] This model is based on a division of an assumed neutrally-stratified flow field into inner and outer layers. The outer layer is characterized by inviscid, potential flow while in the inner layer a balance between advective, pressure-gradient and turbulent-viscous forces is assumed and turbulent transfers are modeled with a simple mixing length closure scheme. Fourier transforms are used to provide the solution. As stated earlier, flow separation cannot be modeled, so terrain slopes are limited to about 25% in order to produce valid solutions. Also, the atmosphere is assumed to be neutrally stratified, which often represents the average conditions on a time scale of months or years, even though actual neutral conditions occur only during a fraction of time. While limited in their applicability, computer codes based on the MS-Micro/3 and similar models like WASP and Wind

Farm have long been the dominant modeling approach for wind resource assessment. Particularly WASP, developed and distributed by Denmark's research center RISØ has been at the heart of wind assessment projects over the last two decades and has been the basis of the European Wind Atlas.

The Mason-Sykes approach, in its three-dimensional version put forward by Jason and Hunt [62], starts with a linearized version of the momentum equation valid in the inner layer written as [62,63]

$$\frac{\partial U}{\partial X} = -\frac{\partial P}{\partial X} + \frac{\partial}{\partial Z} \left(Z \frac{\partial U}{\partial Z} \right) \tag{67}$$

$$\frac{\partial V}{\partial Y} = -\frac{\partial P}{\partial Y} + \frac{1}{2} \frac{\partial}{\partial Z} \left(Z \frac{\partial V}{\partial Z} \right) \tag{68}$$

where $P(X, Y) = p_1(x, y, 0)$ is the outer region pressure at $\Xi = z/L = 0$ and the coordinates X and Y have been normalized to an appropriate horizontal length scale L , i.e., $X = x/L$, $Y = y/L$. $Z = (z - z_s)/l$ is the normalized vertical distance with respect to the local terrain height defined by

$$z_s = hf(x/L, y/L) \tag{69}$$

where h is the highest elevation within the simulation domain, typically a hill height, and a vertical length scale l has been introduced by setting

$$\frac{l}{L} \ln \left(\frac{l}{z_0} \right) = 2\kappa^2 \tag{70}$$

with the von Karman constant κ (usually taken as 0.4); z_0 is the roughness length of the terrain, assumed constant in the original model [62], although subsequent modifications [63] allow for horizontal variations of surface roughness. As stated earlier, the flow in the outer region is modeled as unviscous potential flow, leading to the following equation for the pressure

$$\left(\frac{\partial^2}{\partial X^2} + \frac{\partial^2}{\partial Y^2} + \frac{\partial^2}{\partial \Xi^2} \right) p_1 = 0 \tag{71}$$

Solutions of the model are then obtained by Fourier-transforming the equations for the horizontal wind velocity components U and V in the inner domain and the pressure field in the outer domain and applying appropriate boundary conditions. The Fourier transforms of U and V can then be written as

$$\tilde{U} = \frac{k'^2 \tilde{f}}{(k'^2 + m'^2)^{1/2}} \left(1 - \frac{K_0(\xi)}{K_0(\xi_0)} \right) \tag{72}$$

$$\tilde{V} = \frac{k'm'\tilde{f}}{(k'^2 + m'^2)^{1/2}} \left(1 - \frac{K_0(\xi^*)}{K_0(\xi_0^*)} \right) \tag{73}$$

where K_0 is the modified Bessel function and \tilde{f} is the Fourier transform of the normalized terrain topography $f(X, Y)$.

6.3. Roughness modeling in linearized models

While MS-Micro/3 satisfactorily describes the effect of topography changes under the limitations described above, the effect of roughness changes is not properly accounted for, particularly in coastal regions. An alternative model developed by Sempreviva *et al.* [64] is based on the concept of the Internal Boundary Layer (IBL) [65,66] which develops from the point of change. When there is a roughness change from z_{01} to z_{02} the IBL height h can be defined at a distance x downstream from the change as:

$$0.9 \frac{x}{z_0} = \frac{h}{z_0} \left\{ \ln \left(\frac{h}{z_0} \right) - 1 \right\} \quad (74)$$

where $z_0 = \max(z_{01}, z_{02})$. The change in surface friction velocity between the two regions is then related to the internal boundary layer height by:

$$\frac{(u^*)_2}{(u^*)_1} = \frac{\ln(h/z_{01})}{\ln(h/z_{02})} \quad (75)$$

The boundary layer profile below the IBL height h is then defined by a combination of the outer profile above $0.3h$ and the inner profile below $0.09h$, with a linear variation of the logarithmic wind speed profile between these two points. Therefore, if $u_1(z)$ is the upstream boundary layer profile, and $u_2(z)$ is the profile at a distance x downstream of the change, we have [64]

$$\frac{u_2(z)}{u_1(z)} = 1 \quad \text{for } z > 0.3h \quad (76)$$

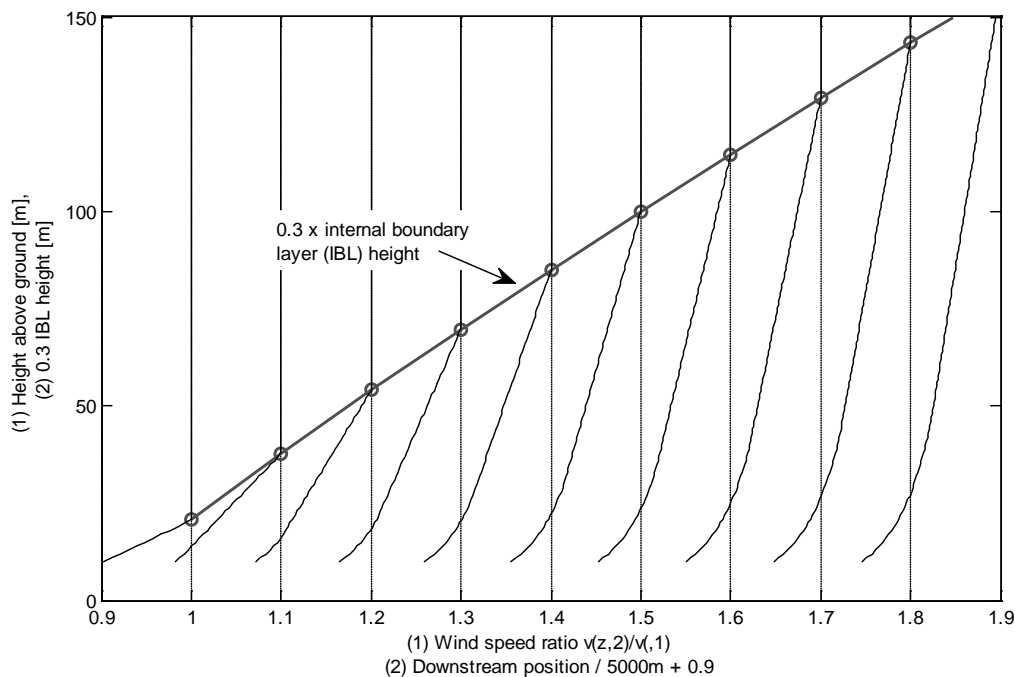
$$\frac{u_2(z)}{u_1(z)} = \frac{\ln(h/z_{01}) \ln(z/z_{02})}{\ln(h/z_{02}) \ln(z/z_{01})} \quad \text{for } z < 0.09h \quad (77)$$

Between these heights (*i.e.*, for $0.09h < z < 0.3h$) a linear variation of the ratio $u_2(z)/u_1(z)$ is assumed. In practice there will be multiple changes in roughness upstream and these can be simply accumulated as:

$$\frac{u_N(z)}{u_1(z)} = \prod_{i=2}^N \frac{u_i(z)}{u_{i-1}(z)} \quad (78)$$

Figure 19 shows how $u_2(z)/u_1(z)$ evolves as a function from the distance of a roughness discontinuity, where the upstream roughness length was $z_{01} = 0.01$ m and the downstream value $z_{02} = 0.1$ m. The horizontal distance increment was 500 m, and adjacent curves have been offset horizontally by 0.1 for clarity. For the purposes of comparison, the function $0.3h(x)$ (where h is the internal boundary layer height) has been overlaid after appropriate scaling. It can be seen from the figure how the slope of the vertical wind speed curve continuously evolves as one moves away from the roughness change in the downstream direction.

Figure 19. Evolution of the ratio of the vertical wind speed profiles before and after a change in roughness length as a function of the distance from the discontinuity. The wind profiles have been offset horizontally for clarity. The evolution of the internal boundary layer has been shown for comparison.



6.4. Full CFD models and turbulence modeling

Reynolds-averaged Navier-Stokes (RANS) models are capable of reproducing many of the features observed for the wind flow in complex terrain; however, for the purposes of predictions it is important to properly adjust the model parameters to account for the details of the atmospheric boundary layer (ABL). Like in many other areas of fluid flow modeling, the starting point are the steady-state incompressible RANS equations given by [67,69]

$$\frac{\partial U_i}{\partial x_i} = 0 \tag{79}$$

$$U_j \frac{\partial U_i}{\partial x_j} = -\frac{1}{\rho} \frac{\partial P}{\partial x_i} + \frac{\partial}{\partial x_j} \left(\nu \left(\frac{\partial U_i}{\partial x_j} + \frac{\partial U_j}{\partial x_i} \right) - \overline{u_i u_j} \right) \tag{80}$$

where upper case letters refer to the average values of the variables, whereas the lower case variables describe the fluctuations. For closure of the equation set a turbulence model is required. Typically, the turbulent Reynolds stresses are related to the mean velocity variables by setting

$$\overline{u_i u_j} = \nu_T \left(\frac{\partial U_i}{\partial x_j} + \frac{\partial U_j}{\partial x_i} \right) + \frac{2}{3} \delta_{ij} k \tag{81}$$

where k is the turbulent kinetic energy and ν_T the turbulent viscosity. Often, the $k-\epsilon$ model is used to provide an expression for the turbulent viscosity in terms of k and its dissipation rate ϵ , as well as transport equations for k and ϵ themselves [67,69]:

$$v_T = c_\mu \frac{k^2}{\varepsilon} \quad (82)$$

$$\frac{\partial}{\partial x_i} (U_i k) = \frac{\partial}{\partial x_i} \left(\frac{v_T}{\sigma_k} \frac{\partial k}{\partial x_i} \right) + P_k - \varepsilon \quad (83)$$

$$\frac{\partial}{\partial x_i} (U_i \varepsilon) = \frac{\partial}{\partial x_i} \left(\frac{v_T}{\sigma_\varepsilon} \frac{\partial \varepsilon}{\partial x_i} \right) + c_{\varepsilon 1} \frac{\varepsilon}{k} P_k - c_{\varepsilon 2} \frac{\varepsilon^2}{k} \quad (84)$$

where the turbulent production term

$$P_k = v_T \left(\frac{\partial U_i}{\partial x_j} + \frac{\partial U_j}{\partial x_i} \right) \frac{\partial U_i}{\partial x_j} \quad (85)$$

has been introduced. It is conspicuous from Equations (82) to (85) that several model parameters have to be determined, either from direct measurements in the ABL or from fine tuning of simulations to measurement of the macroscopic flow variables.

Gravdahl [67] attempted to correct some of the known shortcomings of the k - ε model, such as an overprediction of the turbulent viscosity in the weak shear layer near the surface, by adjusting some of the parameters of k - ε model according to measurements in the atmospheric boundary layer [70]. He then compared the predictions of the standard and the modified model with field measurements conducted at the so-called Askervein hill [71], a famous measurement campaign which has served as test case for many modeling approaches since. The Askervein hill roughly represents an ellipsoid with major and minor axis of 2 km and 1 km, respectively (Figure 19). Comparisons of the measurements and the model output were conducted for the sections A and AA in Figure 20.

Figure 20. Elevation contours and grid distribution for the simulation of the Askervein Hill [67]. *Reproduced with permission* [68].

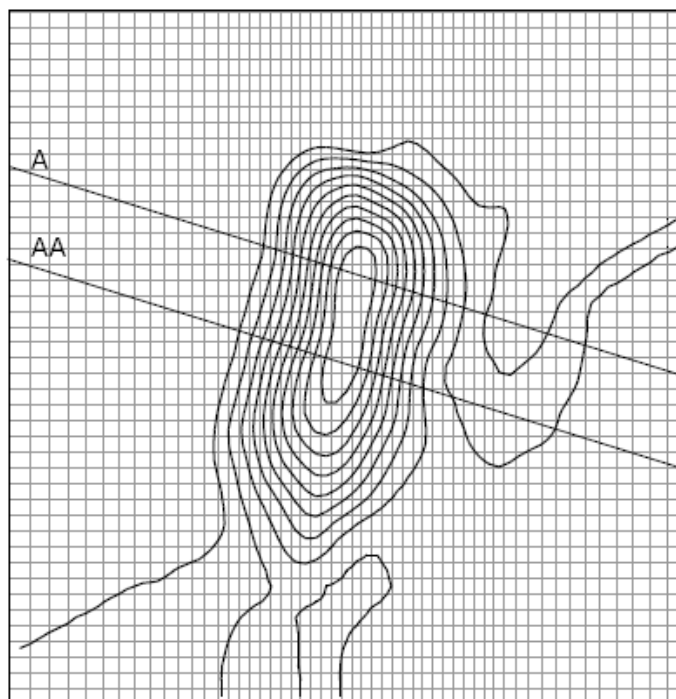
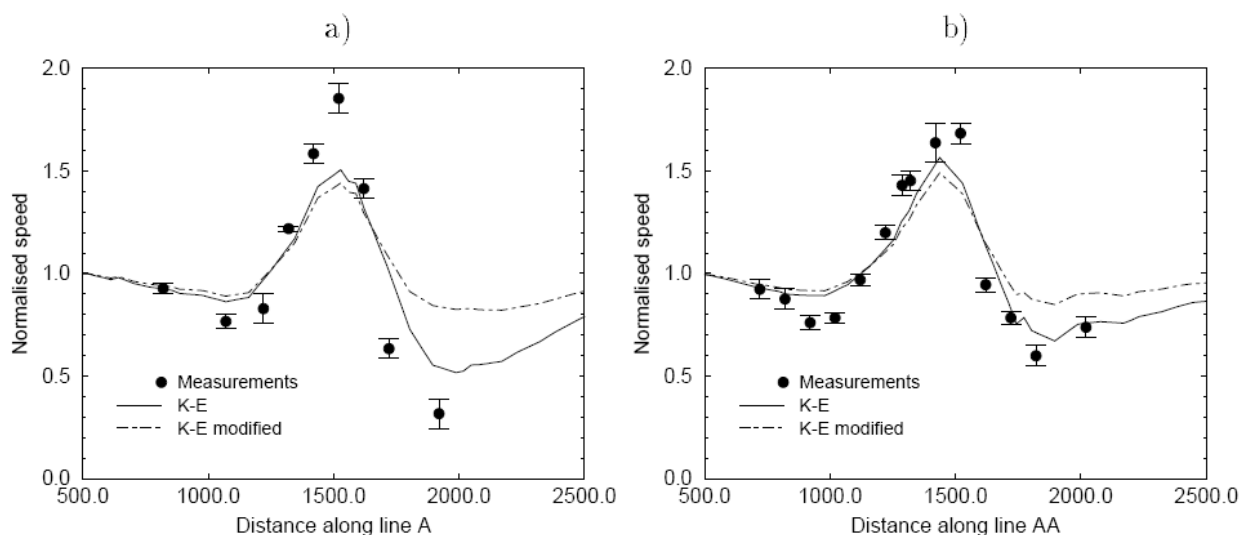


Table 3. k - ε turbulence closure parameters for RANS modeling [67].

	c_μ	σ_k	σ_ε	$c_{\varepsilon 1}$	$c_{\varepsilon 2}$
Standard k - ε model	0.09	1.0	1.3	1.44	1.92
Modified for ABL modeling	0.0324	1.0	1.85	1.44	1.92

As it can be seen from Figure 21, both models provide a good approximation of the speed-up and the reduction of the wind speed at the lee side along line AA, with the standard k - ε model showing a better performance. Along line A both models under-predict the speed-up, and now only the standard k - ε model provides an acceptable prediction of the lee side wind speed. These findings illustrate that often in RANS modeling an improvement in one aspect (in this case the turbulence structure of the weak shear layer near the surface) comes at the expense of a less accurate prediction of other parameters, such as the mean wind speed.

Figure 21. Normalized wind speed over the Askervein Hill for section A (a) and AA (b).
Reproduced with permission [68].



While the Askervein experiment has long served as the reference case, more recently a comprehensive field experiments at the small peninsula Bolund just north of the Danish research center RISØ has provided a new opportunity for testing different computational models [72]. The Bolund hill has a steep edge facing the predominant winds, thereby providing a significant challenge to modeling. A blind comparison campaign was conducted for testing different modeling approaches, including experimental models (wind tunnel, flow channel), linear solvers, RANS and LES [73] (large eddy simulation) approaches. The overwhelming number of contestants used some kind of RANS approach, mostly based on two-equation turbulence closure models, though some one-equation solvers also participated. Groups using linear solvers either used WASP Engineering or a similar program. A few participants used a hybrid RANS/LES approach. It is interesting to observe that no pair of identical results was obtained, although some programs (such as WindSim and WASP) were used by several groups, leading the conclusion that the user is as important as the software tool to obtain meaningful results. The general overall finding was that RANS models outperformed the other approaches, with all

programs used in the top 10 list belonging to the RANS category. Nine of these ten groups used a k- ϵ model, with only one one-equation turbulence closure model appearing in the list. Not unexpectedly, linear models had the largest error and generally fail to predict the speed-up peak. The experimental approaches predicted the mean velocities fairly well, but under-predicted the turbulent kinetic energy. The RANS/LES, finally, showed some potential but a considerable spread was seen among models, indicating that this kind of approach is still immature.

6.5. Roughness modeling in CFD

Surface roughness is often described by the wall roughness model put forward by Cebeci and Bradshaw [74]; see Blocken *et al.* [75] for a more recent discussion. The starting point is the definition of an equivalent Reynolds number K_s^+ built from the effective height of the roughness elements K_s and the friction velocity v_τ :

$$K_s^+ = \frac{\rho K_s u_\tau}{\mu} \quad (86)$$

The flow speed in the vicinity of the wall is then governed by a logarithmic relationship between the dimensionless wind speed u^+ and y^+ :

$$u^+ = \frac{1}{\kappa} \ln(y^+) + B - \Delta B \quad (87)$$

where

$$u^+ = \frac{u}{u_\tau} \quad \text{and} \quad y^+ = \frac{\rho y u_\tau}{\mu} \quad (88)$$

and κ is the von Karman constant (often taken as 0.4) and B is an experimental constant with a typical value of 5.45. ΔB depends on the roughness Reynolds number K_s^+ in the following way:

$$\Delta B = \begin{cases} 0 & K_s^+ \approx 3-5 \\ \frac{1}{k} \ln \left[\frac{K_s^+ - 2.25}{87.75} + C_S K_s^+ \right] \sin \left[0.4358 (\ln K_s^+ - 0.811) \right] & 3-5 < K_s^+ < 70-90 \\ \frac{1}{k} \ln (1 + C_S K_s^+) & K_s^+ > 70-90 \end{cases} \quad (89)$$

Following investigations by Nikuradse [76] in ducts with uniform wall roughness the constant C_S is often taken as 0.5 if k - ϵ turbulence models are used. Commercial CFD codes like Fluent first compute the friction velocity v_τ which is used to evaluate the dimensionless roughness height that is used to calculate ΔB and finally the velocity at the wall adjacent cell by means of equation (87). In order to apply the wall roughness model to wind flow modeling Crasto in his Ph.D. thesis [69] proposes an approximate expression relating the roughness length z_0 with the parameters of the wall roughness model described above:

$$z_0 = C_S K_s \exp(-k B) \quad (90)$$

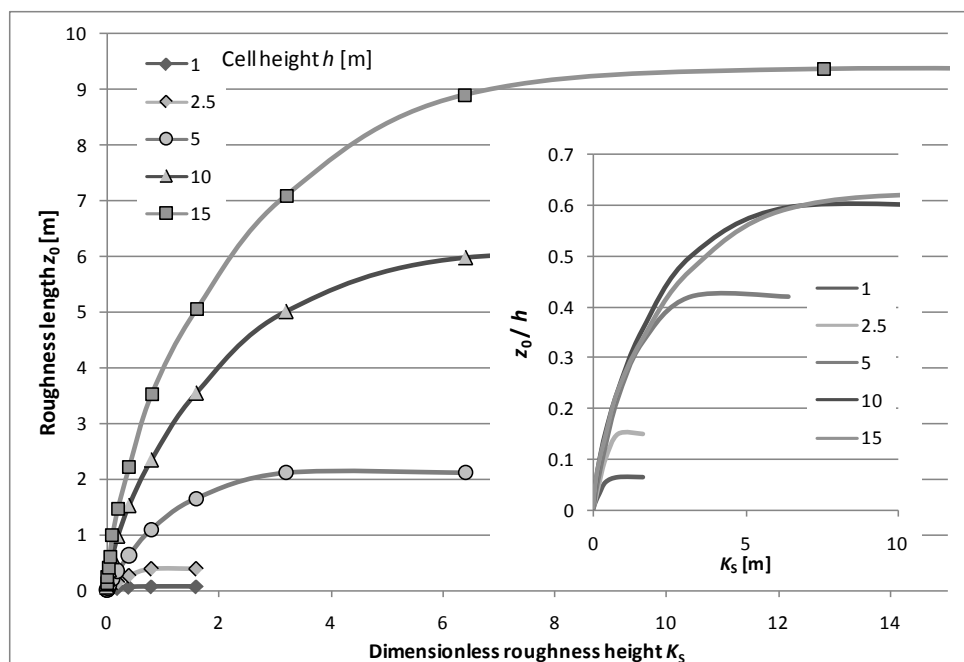
In order to validate his expression Crasto first notes the importance of the height of the grid cells adjacent to the wall and defines seven roughness classes defining a cell height for each class. The

author first evaluates the results obtained for z_0 using the value for K_S suggested by equation (89). He then proceeds to obtain refined values for the effective roughness constant K_s , maintaining a value of $C_s = 1$ in all cases, in order to reproduce the desired value of the roughness length z_0 . In his simulations, the desired logarithmic velocity profile is specified at the inlet of the simulation domain, together with analytical expressions for the turbulent kinetic energy and its dissipation rate. The roughness length of the fully developed atmospheric boundary layer is then evaluated at the outlet of the simulation domain.

While the results obtained by Crasto provide useful guidance for the specification of z_0 in CFD simulations, no information about the development of boundary layer as the fluid moves along the simulation domain is obtained from his results. Moreover, cell height has only been considered as far as the selection of cell size depending on the desired roughness class is concerned. In order to further investigate these issues the authors conducted a series of numerical 2D simulations for a flat surface with constant wall roughness parameters using the commercial CFD solver Fluent. As opposed to Crasto, they did not specify the desired vertical wind speed profile at the domain inlet, but rather specified a constant inlet velocity and allowed the vertical profile to converge. Cell heights were taken to be 1, 2.5, 5, 10, and 15, respectively, where K_S was varied in a geometric progression between 0.00625 and 25.6. The maximum value of K_S in each of the simulations was limited by the height of the cell adjacent to the surface.

It can be seen from Figure 22 that only for small values of K_S an approximately linear relationship between z_0 and K_S exists, while for large values of K_S , z_0 converges to an asymptotic value given by the height of the cell adjacent to the surface. Interestingly, z_0 was found to scale with the cell height as illustrated by the inset of where z_0/h has been plotted against K_S , showing that for small values of K_S all scaled curves coincide, before they level off at higher K_S values.

Figure 22. Relation between roughness length z_0 and the dimensionless roughness height K_s for different heights of the grid cell adjacent to the surface. *Inset:* Roughness length normalized by the cell height.



From these findings it can be concluded that caution should be taken when modeling surface roughness in CFD, since generally both the wall roughness and the height of the cell adjacent to the surface are important. Fortunately, for small values of K_S the scaled roughness length z_0/h is a function of K_S alone. It is also evident, however, that the wall roughness model is only appropriate as long as the cell height is large compared to the roughness length, imposing a certain trade-off between the modeling of small topographic features and surface roughness.

6.6. The effect of topography on wind shear

Not surprisingly, vertical wind shear not only depends on surface roughness, but also on the topographic features of the terrain. Especially in complex terrain the departure from the logarithmic wind speed profile may be significant, and even where an approximately logarithmic variation exists, the apparent values of the roughness length may be substantially different from the flat plane values. In order to explore this issue, a one-dimensional test geometry consisting of an extended mesa with symmetric up- and downwind edges was modeled and simulated with the commercial CFD solver Fluent [77]. Both edges were modeled by error functions $\text{erf}(x)$ with the maximum slope S as the free parameter. The following RANS parameters were used for the simulation: $C_m = 0.09$, $C_{1-e} = 1.444$, $C_{2e} = 1.92$, Energy Prandtl Number = 0.85, TDR Prandtl Number = 1.3, TKE Prandtl Number = 1, Wall Prandtl Number = 0.85. The total domain length was 15 km, and the length of the mesa was fixed at 500 m.

As shown in Figure 23(a), where the vertical variation of the wind speed as a function of the previously defined wall roughness constant K_S has been plotted for a location close to the leading edge of the mesa, the wind speed increases rapidly with height, reaching a maximum at a height of approximately 150 m for most values of the roughness parameter and then decreases to converge against the geostrophic value of the wind speed.

While the complete profile has a fairly complex behavior, $v(z)$ can be parameterized in terms of a logarithmic profile with an apparent roughness length for heights of up to about 100 m, except for very low values of K_S . These apparent values of the roughness length have been plotted in Figure 23(b) for different locations on the mesa as a function of the slope parameter S and a fixed value of the roughness parameter K_S . The free-stream roughness length was $z_0 = 0.8$ m in all cases. As shown by Figure 23(b) the apparent roughness length is lower at the leading edge than at the corresponding symmetric positions near the trailing edge. Moreover, a significant reduction of apparent roughness with increasing values of the slope parameter is evident from the figure. Also, while at small values of S all curves tend to converge, at high values a more substantial differentiation between the leading and trailing edge situations occurs. The general decrease in wind shear for wind flow over the mesa can be understood in terms of a compactation of the flow lines as the air is forced to flow uphill. Note that this effect is less pronounced on the trailing edge, where the flow lines tend to detach from the surface, particularly at higher values of the slope parameter.

Figure 23. Vertical wind shear profiles for wind flow over symmetric mesa structures as determined with a commercial CFD tool (Fluent). (a) Vertical profiles at the leading edge of the mesa for different values of the wall roughness parameter $H (=K_S)$. (b) Effective roughness length at different positions on the mesa as a function of the average edge slope S . The free-stream roughness length was fixed at $z_0 = 0.8$ m.

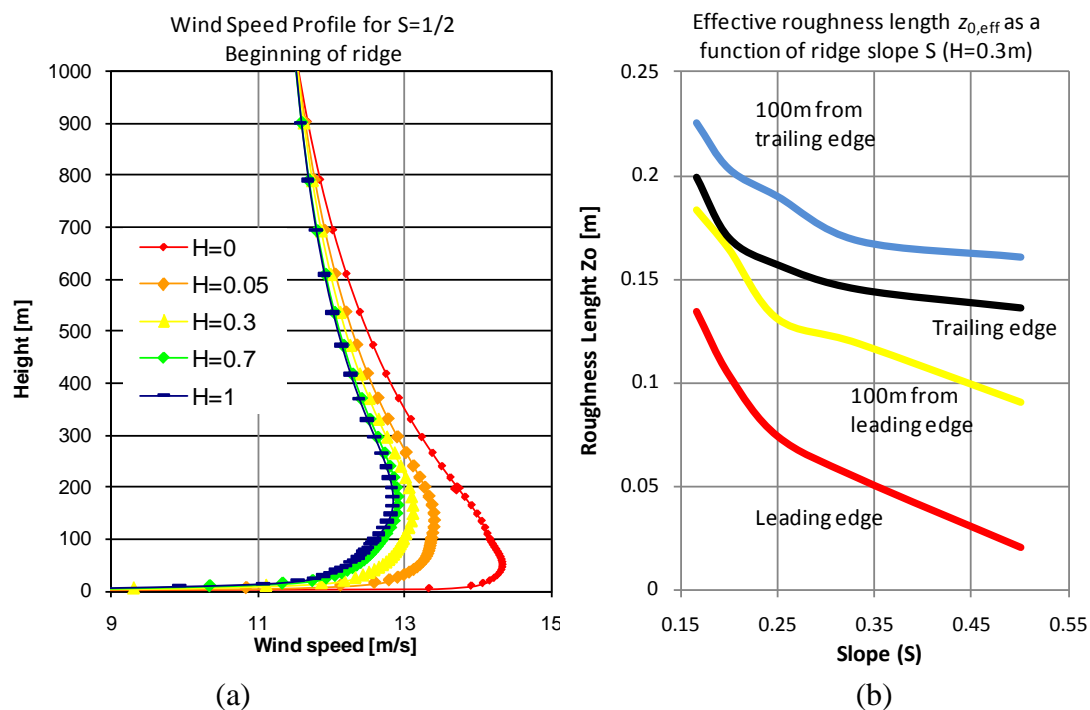
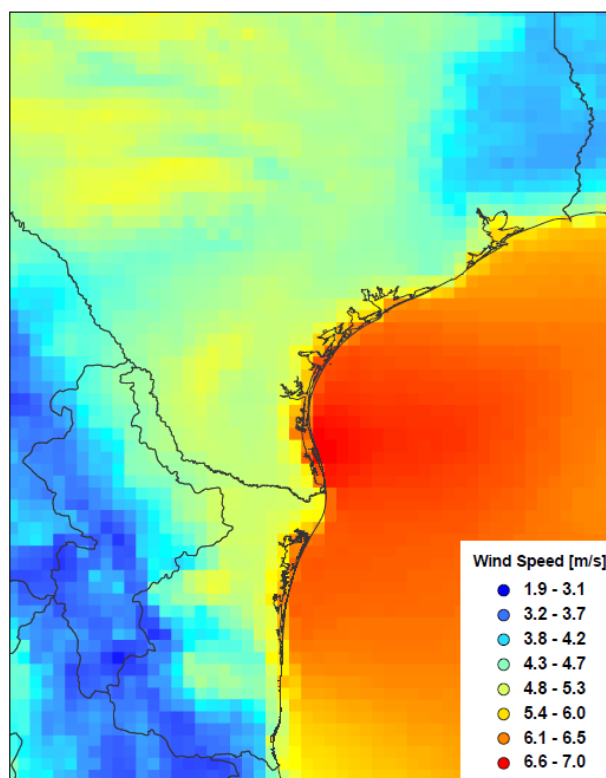


Figure 24. Surface wind speed map (10 m) for Southern Texas and Northeastern Mexico created from the North American Mesoscale (NAM) Model output for one year.



6.7. Mesoscale modeling

While CFD techniques are useful for creating wind maps on a scale typical for wind farm developments (up to a few tens of kilometers), extrapolations beyond this scale generally run into discrepancies due to the variation of the micro-climate. Meteorological models, on the other hand, like the ones used for numerical weather prediction (NWP) are capable of making accurate predictions for temperature, pressure, dew point and other primary weather parameters based on detailed models of the atmospheric physics and are natural candidates when tools for meso scale maps (Figure 24), *i.e.*, maps on length scales of the order of 100 km are required.

Due to the great number of variables considered, NWP computations are still quite time consuming, even with today's computing power. A typical regional NWP prediction for one time interval requires a few hours of computation time on a dual core 2 GHz PC running under Linux for a grid resolution of about 20 km. Due to the limited resolution of such predictions and the local nature of the driving forces for the creation of wind, it cannot be expected that local wind speeds will be predicted accurately by NWP models. However, given the large body of information readily available from public data sources, it is convenient to study the usefulness of directly using NWP model output for wind resource assessment purposes.

In order to evaluate the usefulness of directly using the output of the NWP model run by the National Weather Service (US) for wind resource assessment, a series of virtual wind towers were constructed through interpolation of North American Model (NAM) [51] predictions to the locations operated by the Texas Coastal Oceanic Observation Network (TCOON). The predictions for wind speed and air temperature were then compared to the observations on a bin-wise basis. Prior to comparison the observational data were slightly filtered to account for downtimes and any other data quality issues. In Figure 25 a bin-wise comparison of the wind speed measured at the TCOON station "Bob Hall Pier" with the corresponding NAM predictions is shown for the year 2008. It is evident from the figure that for the predominant wind speed intervals from 3 to 9 m/s, concentrating over 70% of all TCOON observations a relatively good agreement was obtained, while the high wind speed events are generally underpredicted. Low wind speed events, on the other hand, were overpredicted by the numerical weather model. Not unexpectedly, as evidenced by Figure 26, the predictions for air temperature are significantly better, with a good agreement in all bins.

Due to the coastal location of the TCOON stations the possibility was considered that the numerical weather prediction model does not adequately model the sea breeze conditions frequently occurring at the coast and often providing the most important driving force for the generation of coastal winds. In order to assess this possibility, wind speed data were categorized by the value of the air-sea temperature difference $\Delta T_{\text{air-sea}}$, where sea breeze conditions were considered to occur if $\Delta T_{\text{air-sea}} > x$ °C. As shown in Figure 27, the average wind speed difference for the period studied (May 1st through July 31st, 2008) was close to zero in both cases, with no difference occurring between sea breeze and non-sea breeze conditions, showing that the numerical weather models adequately predicts both situations.

Figure 25. Boxplot showing the differences between measured and predicted wind speed values for the TCOON site “Bob Hall Pier” for different wind speed bin intervals. The measured (TCOON) wind speed histogram is shown for comparison.

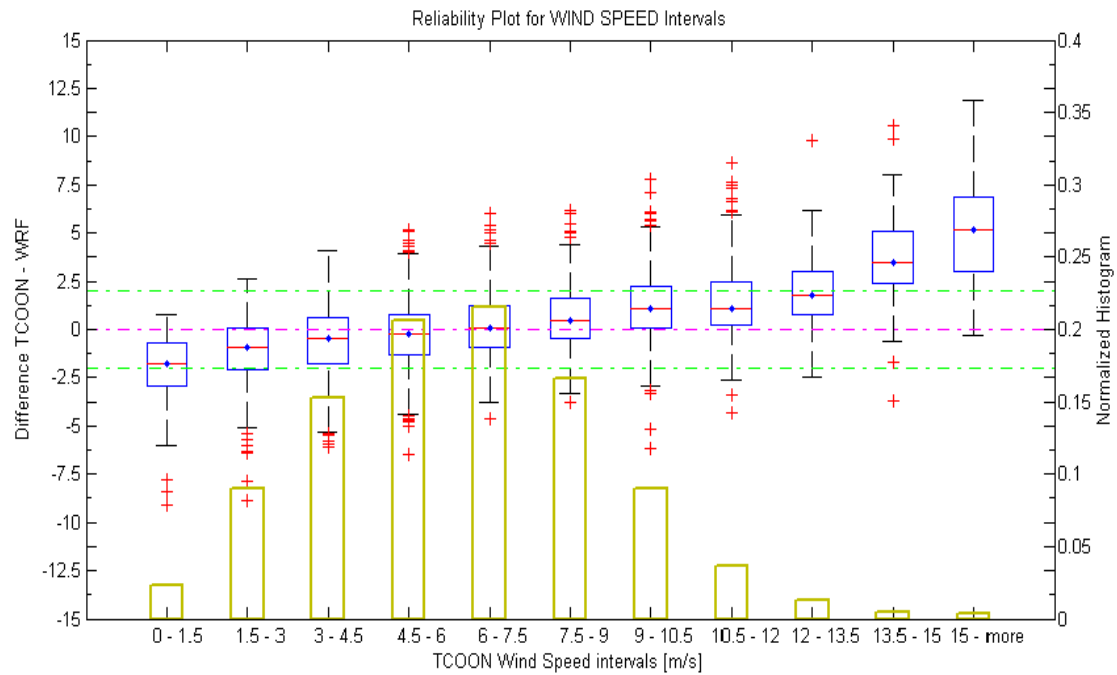


Figure 26. Boxplot showing the differences between measured and predicted temperature values for the TCOON site “Bob Hall Pier” for different air temperature bin intervals. The measured (TCOON) temperature histogram is shown for comparison.

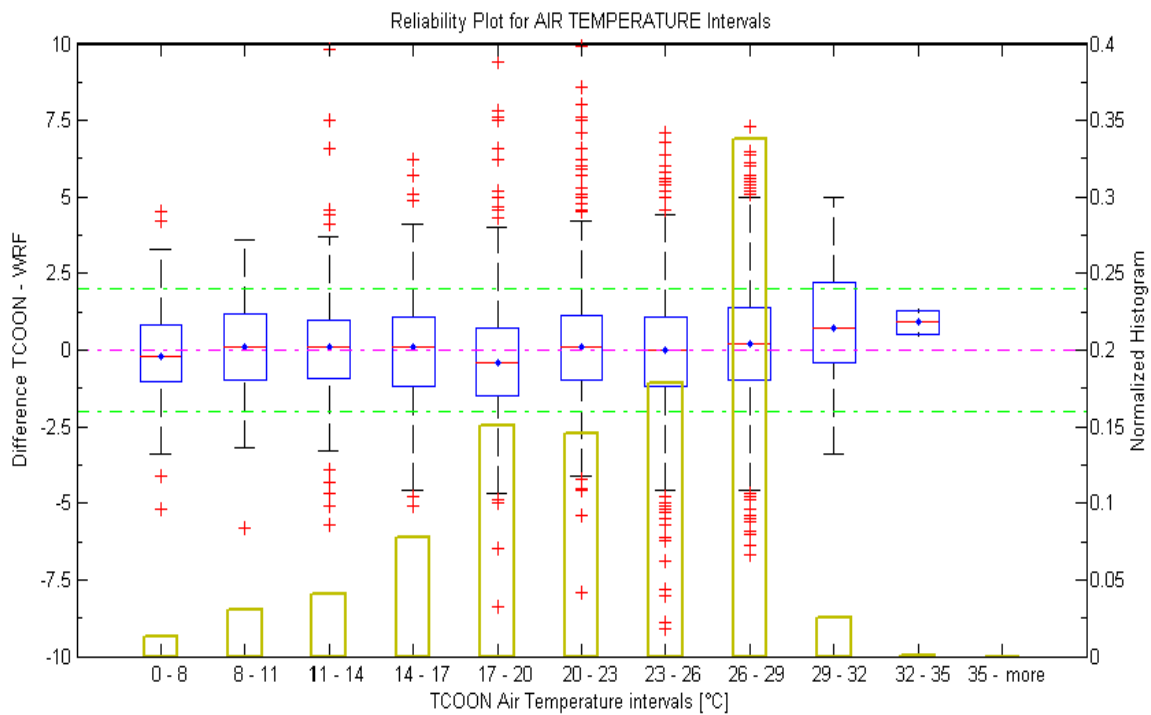
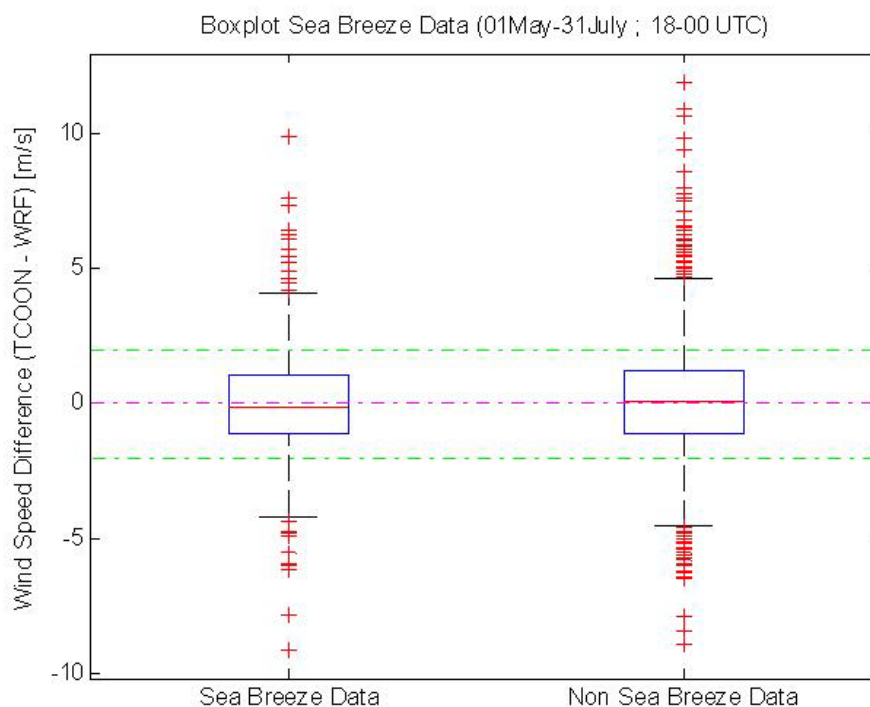


Figure 27. Boxplots for overall wind speed differences of the measured and the predicted values for both sea breeze conditions (left box of each graph) and non-sea breeze conditions.



In recent years, considerable effort has been put in the refinement of NWP models for the purpose of wind speed modeling. The general approach consists in a nesting sequence where relatively coarse maps generated from general circulation models (GCM) provide the boundary conditions for mesoscale maps which are consecutively refined down to a scale (~ 100 m) useful for micrositing efforts on a wind farm level. Each simulation output serves for the initialization of the subsequent simulation.

A typical starting point for such a simulation is a 20- to 30-year data set extracted from the NCEP/NCAR (NCEP = National Center for Environmental Prediction, NCAR = National Center for Atmospheric Research) reanalysis data base [52] with a resolution of $2.5^\circ \times 2.5^\circ$. This data base contains four daily values corresponding to 00, 06, 12 and 18 hours UTC. In a subsequent step a mesoscale NWP model such as the ARW-WRF is run on an hourly basis in the non-hydrostatic configuration and a $0.2^\circ \times 0.2^\circ$ resolution for a 20- to 30-year period. In the final step, a high resolution ($0.03^\circ \times 0.03^\circ$) simulation for 24 hours/day but a shorter period, say, 5–10 years is conducted. While in principle the long-term wind resource at a potential wind farm development site can be predicted without the need for local measurements, the quality of the predictions is ultimately limited by the quality of the data used to initialize the simulations, typically reanalysis data [52]. While reanalysis data are considered the best guess for the climatology in a given region, their accuracy still depends on weather data collected locally, e.g., through ASOS stations or balloon measurements. Therefore, mesoscale simulations cannot be expected to make on-site measurements unnecessary, particularly in the many regions of the world where long-term meteorological measurements are scarce and of uncertain quality. Fortunately, the ongoing progress in numerical weather prediction modeling through better numerical models not requiring parametrizations and coupling between ocean, land and

atmosphere, improvements in the quality of the observational data, and better data assimilation schemes (see [77] for a review of these topics) can be expected to provide a useful spin-off for more accurate wind resource assessment in the near future.

7. Summary and Conclusions

The field of wind resource assessment is evolving rapidly, responding to the increasingly stringent requirements of large-scale wind farm projects often involving investments of several hundred million dollars. Traditional cup anemometry is being complemented with ultrasonic sensors providing information on all three components of the wind velocity vector and enabling a better assessment of turbulence. Remote sensing devices like sodar and lidar are becoming more popular as turbine hub heights and rotor diameters increase, often placing the upper edge of the swept rotor area at heights of 130 m or more. While the traditional approach of measuring the wind speed at a few heights below hub height and extrapolating based on a logarithmic profile is still very common, the use of both vertical profiling devices and more accurate modeling tools considering the full terrain complexity and atmospheric stability is quickly moving into the mainstream. Mesoscale modeling tools based on the full consideration of the physics of the atmospheric boundary layer and borrowed from meteorology are increasingly used for early prospection, particularly in areas of the world without a dense network of reliable monitoring stations, and for the long-term assessment through correlation of virtual wind tower data with on-site recorded wind data, complementing the traditional approach of correlating with automated surface stations

Acknowledgements

The financial support of Tecnológico de Monterrey through funding of the research chair for wind energy (contract number CAT158) is gratefully acknowledged. We also appreciate the help of Roberto Chávez with the mesoscale simulations and José Francisco Herbert with CFD calculations. The authors would also like to thank Philippe Tissot at Texas A&M University in Corpus Christi and Waylon Collins at the National Weather Service in Corpus Christi for their collaboration. Useful comments by Javier Amezcua helped improve the manuscript. Finally, and certainly not least, we thank American Shoreline Inc. for continuous support and encouragement.

References and Notes

1. Clifford, S.; Blanco, I.; Kjaer, Ch. Wind at Work. Wind Energy and Job Creation in the EU. European Wind Energy Association, 2009. Available online: http://www.ewea.org/fileadmin/ewea_documents/documents/publications/Wind_at_work_FINAL.pdf (accessed on 13 May 2010).
2. Annual Wind Industry Report 2009. American Wind Energy Association, 2009. Available online: <http://www.awea.org/publications/reports/AWEA-Annual-Wind-Report-2009.pdf> (accessed on 13 May 2010).
3. European Wind Energy Council. Available online: <http://www.erec.org/renewableenergysources/wind-energy.html> (accessed on 13 May 2010).

4. Wisser, R.; Bolinger, M. Annual Report on U.S. Wind Power Installation, Cost, and Performance Trends: 2007, US Department of Energy, Energy Efficiency and Renewables, May 2008. Available online: <http://www1.eere.energy.gov/windandhydro/pdfs/43025.pdf> (accessed on 13 May 2010).
5. Kristensen, L.; Hansen, O.F. *Distance Constant of the Risø Cup Anemometer*; Report Number Risø-R-1320 (EN), RISØ: Roskilde, Denmark, 2002.
6. Kristensen, L. The perennial cup anemometer. *Wind Energy* **1999**, *2*, 59–75.
7. Wyngaard, J.C. Cup, propeller, vane, and sonic anemometers in turbulence research. *Ann. Rev. Fluid Mech.* **1981**, *13*, 399–423.
8. Pedersen, B.M.; Pedersen, T.F.; Klug, H.; van der Borg, N.; Kelley, N.; Dahlberg, J.A. *Recommended Practices for Wind Turbine Testing and Evaluation. 11. Wind Speed Measurement and Use of Cup Anemometry*; Hunter, R.S., Ed.; International Energy Agency: Paris, France, 2003.
9. Hansen, M.O.L.; Pedersen, B.M. Influence of the meteorology mast on a cup anemometer. *J. Solar Energy Eng.* **1999**, *21*, 128–130.
10. Kaimal, J.C.; Gaynor, J.E.; Zimmerman, H.A.; Zimmerman, G.A. Minimizing flow distortion errors in a sonic anemometer. *Bound.-Lay. Meteorol.* **1990**, *53*, 103–115.
11. Wilczak, J.M.; Oncley, S.P.; Stage, S.A. Sonic anemometer tilt correction algorithms, *Bound.-Lay. Meteorol.* **2001**, *99*, 127–150.
12. Cuerva, A.; Sanz-Andrés, A. On sonic anemometer measurement theory. *J. Wind Eng. Ind. Aerodyn.* **2000**, *88*, 25–55.
13. Kaimal, J.C.; Wyngaard, J.C.; Haugen, D.A. Deriving power spectra from a three-component sonic anemometer, *J. Appl. Meteorol.* **1968**, *7*, 827–837.
14. Crescenti, G.H. The degradation of doppler sodar performance due to noise: A review. *Atmos. Environ.* **1998**, *32*, 1499–1509.
15. Anderson, P.S.; Ladkin, R.S.; Renfrew, I.A. An autonomous doppler sodar wind profiling system. *J. Atmosph. Ocean. Technol.* **2005**, *22*, 1310–1325.
16. Keder, J.; Foken, Th.; Gerstmann, W.; Schindler, V. Measurement of wind parameters and heat flux with the sensitron Doppler SODAR, *Bound.-Lay. Meteorol.* **1989**, *46*, 195–204.
17. Ormel, F.; Bradley, S.; von Hünerbein, S.; Emeis, S.; Warmbier, G. *On the Theory of SODAR Measurement Techniques*. Antoniou, I., Jørgensen, H.E., Eds.; Report No. Risø-R-1410 (EN), RISØ: Roskilde, Denmark, April 2003.
18. Pérez; I.A.; García, M.A.; Sánchez, M.L.; de Torre, B. Analysis of height variations of sodar-derived wind speeds in Northern Spain. *J. Wind Eng. Ind. Aerodyn.* **2004**, *92*, 875–894.
19. Coulter, R.L.; Wesely, M.L. Estimates of surface heat flux from sodar and laser scintillation measurements in the unstable atmospheric boundary layer. *J. Appl. Meteor.* **1980**, *19*, 1209–1222.
20. Guedelia, D.; Ntsila A.; Druilhet, A.; Fontan, J. Monitoring of the atmospheric stability above and urban and suburban site using sodar and radon measurements. *J. Appl. Meteor.* **1980**, *19*, 839–848.
21. Neal, B. Personal communication, May 21, 2010.
22. de Baas, A.; Sarazin, M. The temperature structure function for complex terrain. In Proceedings of the Eighth Symposium on Turbulent Shear Flows, Munich, Germany, 9–11 September 1991.

23. Peters, G.; Wamser, C.; Hinzpeter, H. Acoustic doppler and angle of arrival detection and comparisons with direct measurements at a 300 m mast. *J. Appl. Meteor.* **1978**, *17*, 1172–1178.
24. Short, D.A.; Wheeler, M.M. *MiniSODAR™ Evaluation*. NASA Contractor Report NASA/CR-2003-211192, NASA: Melbourne, FL, USA, 2003.
25. Henson, W.L.W.; Rogers, A.L.; Manwell, J.F. Wind resource assessment using SODAR at cluttered sites. In European Wind Energy Conference, Athens, Greece, 27 February–2 March 2006.
26. Walls, E.; Rogers, A.L.; Manwell, J.F. *Eastham, MA: SODAR-Based Wind Resource Assessment*; Renewable Energy Research Laboratory, University of Massachusetts: Amhurst, MA, USA, 2007.
27. Jaynes, D.W.; Manwell, J.F.; McGowan, J.G.; Stein, W.M.; Rogers, A.L. *MTC Final Progress Report*; LIDAR, Renewable Energy Research Laboratory, University of Massachusetts: Amhurst, MA, USA, 2007.
28. Liu, Z.S.; Liu, B.Y.; Wu, S.H.; Li, A.G.; Wang, A.J. High spatial and temporal resolution mobile incoherent Doppler lidar for sea surface wind measurements. *Optics Letters* **2008**, *33*, 1485–1486.
29. Antoniou, I.; Courtney, M.; Jørgensen, H.E.; Mikkelsen, T.; von Hünerbein, S.; Bradley, S.; Piper, B.; Harris, M.; Marti, I.; Aristu, M.; Foussekis, D.; Nielsen, M.P. Remote sensing the wind using Lidars and Sodars. In Proceedings of the European Wind Energy Conference, Milan, Italy, May 2007.
30. Bingöl, F.; Mann, J.; Foussekis, D. Lidar performance in complex terrain modelled by WASP engineering. In Proceedings of the European Wind Energy Conference. Marseille, France, March 2009.
31. Bingöl, F. Personal communication. 24 January 2010.
32. Pedersen, B.M.; Brinch, M.; Fabian, O. Some experimental investigations on the influence of the mounting arrangements on the accuracy of cup anemometer measurements. *J. Wind Eng. Ind. Aerodyn.* **1992**, *39*, 373–383.
33. Simiu, E.; Scanlan, R.H. *Wind Effects on Structures*, 3rd ed.; John Wiley & Sons: New York, NY, USA, 1996.
34. Petersen, E.L.; Mortensen, N.G.; Landberg, L.; Højstrup, J.; Frank, H.P. Wind power meteorology. Part I: climate and turbulence. *Wind Energy* **1998**, *1*, 2–22.
35. Venkatram, A. Estimating the Monin-Obukhov length in the stable boundary layer for dispersion calculations *Bound.-Layer Meteor.* **1980**, *19*, 481–485.
36. Tieleman, H.W. Roughness estimation for wind-load simulation experiments. *J. Wind Eng. Ind. Aerodyn.* **2003**, *91*, 1163–1173.
37. Barthelmie, R.J.; Palutikof, J.P.; Davies, T.D. Estimation of sector roughness lengths and the effect on prediction of the vertical wind speed profile. *Bound.-Lay. Meteorol.* **1993**, *66*, 19–47.
38. Wieringa, J. Representative roughness parameters for homogeneous terrain. *Bound.-Lay. Meteorol.* **1993**, *63*, 323–363.
39. Wieringa, J. Updating the Davenport terrain roughness classification, *J. Wind Eng. Ind. Aerodyn.* **1992**, *41*, 357–368.
40. Verkaik, J.W. Evaluation of two gustiness models for exposure correction calculations. *J. Appl. Meteor.* **2000**, *39*, 1613–1626.

41. Koo, E.; Chang, W.L.; Lee, B.Y. An alternate stability classification scheme for air quality modeling. In Proceedings of the 4th Conference on Air Pollution Meteorology, Portland,, October 1984.
42. Andersen, M. *A Review of MCP Techniques*; Report No. 01327R00022, Renewable Energy Systems: UK, July 2004.
43. Derrick, A. Development of the measure-correlate-predict strategy for site assessment. In Proceedings of the European Wind Energy Conference EWEC, Lübeck-Travemünde, Germany, March 1993.
44. Rogers, A.L.; Rogers, J.W.; James, F.; Manwell, J.F. Comparison of the performance of four measure–correlate–predict algorithms. *J. Wind Eng. Ind. Aerodyn.* **2005**, *93*, 243–264.
45. Woods, J.C.; Watson, S.J. A new matrix method for predicting long-term wind roses with MCP. *J. Wind Eng. Ind. Aerodyn.* **1997**, *66*, 85–94.
46. Romo, A.; Amezcua, J.; Probst, O. Validation Of A New MCP Method Using Data From Coastal Sites In Texas, In Proceedings of Wind Power 2009, American Wind Energy Association, Chicago, IL, USA, 4–7 May 2009.
47. Texas Coastal Oceanic Observation Network, Division of Near-Shore Research, Texas A&M University Corpus Christi. Available online: <http://lighthouse.tamucc.edu/TCOON/HomePage> (accessed on 13 May 2010).
48. Parlange, M.B.; Brutsaert, W. Regional shear stress of broken forest from radiosonde wind profiles in the unstable surface layer. *Bound.-Lay. Meteorol.* **1993**, *64*, 355–368.
49. Horstmann, J.; Koch, W.; Lehner, S.; Tonboe, R. Wind retrieval over the ocean using synthetic aperture radar with C-band HH polarization. *IEEE Trans. Geosci. Remote Sensing* **2000**, *38*, 2122–2131.
50. Harris, R.I. The macrometeorological spectrum—A preliminary study. *J. Wind Eng. Ind. Aerodyn.* **2008**, *96*, 2294–2307.
51. Ek, M.B.; Mitchell, K.E.; Lin, Y.; Rogers, E.; Grunmann, P.; Koren, V.; Gayno, G.; Tarpley, J.D. Implementation of Noah land surface model advances in the National Centers for Environmental Prediction operational mesoscale Eta model. *J. Geophys. Res.* **2003**, *108*, 8851.
52. Mesinger, F.; DiMego, G.; Kalnay, E.; Mitchell, K.; Shafran, P.C.; Ebisuzaki, W.; Jović, Woollen, D.J.; Rogers, E.; Berbery, E.H.; Ek, M.B.; Fan, Y.; Grumbine, R.; Higgins, W.; Li, H.; Lin, Y.; Manikin, G.; Parrish, D.; Shi, W. North American regional reanalysis. *Bullet. Amer. Meteorol. Soci.* **2006**, *87*, 343–360.
53. Liu, H. *Wind Engineering. A Handbook for Structural Engineers*; Prentice Hall: Englewood Cliffs, NJ, USA, 1991.
54. Harris; R.I. Gumbel re-visited—A new look at extreme value statistics applied to wind speeds. *J. Wind Eng. Ind. Aerodyn.* **1996**, *59*, 1–22.
55. Cook, N.J.; Harris, R.I.; Whiting, R. Extreme wind speeds in mixed climates revisited. *J. Wind Eng. Ind. Aerodyn.* **2003**, *91*, 403–422.
56. Makkonen L. Bringing closure to the plotting position controversy. *Comm. Stat. Theor. Meth.* **2008**, *37*, 460–467.
57. Gringorten, I.I. A plotting rule for extreme probability paper. *J. Geophys. Res.* **1963**, *68*, 813–814.

58. Gumbel, E.J. *Statistics of Extremes*; Columbia University Press: New York, NY, USA, 1958.
59. Oliver, M.A.; Webster, R. Kriging: A method of interpolation for geographical information systems. *Int. J. Geogr. Inf. Sys.* **1990**, *4*, 313–332 .
60. Mann, J.; Ott, S.; Jørgensen, B.H.; Frank, H.P. *WAsP Engineering 2000*. Report No. Risø-R-1356 (EN) RISØ: Roskilde, Denmark, 2002.
61. Kiranoudis, C.T.; Voros, N.G.; Maroulis, Z.B. Short-cut design of wind farms. *Energy Policy* **2001**, *29*, 567–578.
62. Walmsley, J.L.; Salmon, J.R.; Taylor, P.A. On the application of a model of boundary-layer flow over low hills to real terrain. *Bound.-Lay. Meteorol.* **1982**, *23*, 17–46.
63. Walmsley, J.L., Taylor, P.A.; Keith, T. A simple model of neutrally stratified boundary-layer flow over complex terrain with surface roughness modulations—MS3DJH/3R. *Bound.-Lay. Meteorol.* **1986**, *36*, 157–186.
64. Sempreviva, A.M.; Larsen, S.E.; Mortensen, N.G.; Troen, I. *Roughness Change for Small and Large Fetches*; Report No. Risø-M-2749, RISØ: Roskilde, Denmark, 1988.
65. Garratt, J.R. The internal boundary layer—A review. *Bound.-Lay. Meteorol.* **1990**, *50*, 171–203.
66. Barthelmie, R.J.; Palutikof, J.P. Coastal wind speed modelling for wind energy applications, *J. Wind Eng. Ind. Aerodyn.* **1996**, *62*, 213–236.
67. Gravdahl, A.R. Meso scale modeling with a Reynolds Averaged Navier-Stokes Solver. In Proceedings of the 31th IEA Experts Meeting—State of the Art of Wind Resource Estimation, Risø, Denmark, October 1998.
68. Gravdahl, A.R. Personal communication, October 19, 2008.
69. Crasto, G. *Numerical Simulations of the Atmospheric Boundary Layer*. Ph.D. thesis, Università degli Studi di Cagliari, Cagliari, Italy, 2007.
70. Panofsky, H.A.; Tennekes, H.; Lenschow, D.H.; Wyngaard, J.C. Characteristics of turbulent velocity components in the surface layer under convective conditions. *Bound.-Lay. Meteorol.* **1977**, *11*, 355–361.
71. Taylor, P.A.; Teunissen, H.W. The Askervein Hill project: overview and background data. *Bound. Layer Meteor.* **1987**, *39*, 15–39.
72. Bechmann, A.; Berg, J.; Courtney, M.S.; Jørgensen, H.E.; Mann, J.; Sørensen, N.N. *The Bolund Experiment: Overview and Background*. Report No. Risø-R-1658(EN), RISØ: Roskilde, Denmark, July 2009.
73. Bechmann, A.; Sørensen, N.N. Hybrid RANS/LES method for wind flow over complex terrain. *Wind Energy* **2010**, *13*, 36.
74. Cebeci T.; Bradshaw. P. *Momentum Transfer in Boundary Layers*; Hemisphere: New York, NY, USA, 1977.
75. Blocken, B.; Carmeliet, J.; Stathopoulos, T. CFD evaluation of wind speed conditions in passages between parallel buildings—Effect of wall-function roughness modifications for the atmospheric boundary layer flow. *J. Wind Eng. Ind. Aerodyn.* **2007**, *95*, 941–962.
76. Nikuradse, J. Tech. Rep. NACA Technical Memorandum 1292. *Strömungsgesetz in rauhen Röhren, vDI Forschungshefte 361 (English translation: Laws of flow in rough pipes)*; National Advisory Commission for Aeronautics: Washington, DC, USA, 1950.

77. Herbert, J.F.; Cárdenas, D.; Probst, O. CFD Modeling of the Wind Flow over Mesa Structures typically found in the Southern US. In Proceedings of the Wind Power 2009, American Wind Energy Association, Chicago, IL, USA, 4–7 May, 2009.
78. Kalnay, E. *Atmospheric Modeling, Data Assimilation and Predictability*; Cambridge University Press: Cambridge, UK, 2010.

© 2010 by the authors; licensee MDPI, Basel, Switzerland. This article is an Open Access article distributed under the terms and conditions of the Creative Commons Attribution license (<http://creativecommons.org/licenses/by/3.0/>).